UNIVERSITY OF CALIFORNIA,
IRVINE

Non-Standard Lore in Dark Matter and Baryogenesis

DISSERTATION

submitted in partial satisfaction of the requirements
for the degree of

DOCTOR OF PHILOSOPHY

in Physics

by

Jason H Arakawa

Dissertation Committee:
Professor Timothy M.P. Tait, Chair
Professor Arvind Rajaraman
Professor Mu-Chun Chen

2022

DEDICATION

For Kira

TABLE OF CONTENTS

LIST OF FIGURES

Page

ACKNOWLEDGMENTS

First and foremost, I would like to thank and express my love to my wife, Kira. The love and support she has shown me cannot be overstated, and I am truly grateful for her unending help and reassurance. I would not be where I am today without her.

I would like to thank my advisor, Tim Tait, for his guidance throughout my time at UCI, and for fostering a very friendly learning environment. I would also like to thank Mu-Chun Chen, Jonathan Feng, Arvind Rajaraman, Michael Ratz, and Yuri Shirman for their continued support and encouragement, as well as the great education and knowledge I received from them.

This work received support in part by NSF Grant No. PHY-1620638, and NSF Grant No. PHY-1915005.

VITA

Jason H Arakawa

EDUCATION

Doctor of Philosophy in Physics **2022**
University of California, Irvine *Irvine, CA*

Bachelor of Science in Physics **2017**
Central Washington University *Ellensburg, WA*

RESEARCH EXPERIENCE

Graduate Research Assistant **2017–2022**
University of California, Irvine *Irvine, California*

TEACHING EXPERIENCE

Teaching Assistant **2017–2022**
University of California, Irvine *Irvine, CA*

Instructor **2021**
University of California, Irvine *Irvine, CA*

REFEREED JOURNAL PUBLICATIONS

Emergent Solution to the Strong CP Problem **2019**
Physical Review Letters

Is a Miracle-less WIMP Ruled Out? **2021**
SciPost Physics

First neutrino interaction candidates at the LHC **2021**
Physical Review D

Annihilogenesis **2022**
Submitted to JHEP

ABSTRACT OF THE DISSERTATION

Non-Standard Lore in Dark Matter and Baryogenesis

By

Jason H Arakawa

Doctor of Philosophy in Physics

University of California, Irvine, 2022

Professor Timothy M.P. Tait, Chair

Many mysteries in particle physics have hinted at physics beyond the standard model. The microscopic identity of dark matter and the origin of the matter-antimatter asymmetry have been elusive, despite the efforts throughout the years in probing the rich space of theories and models. To be able to map out the possibilities thoroughly, it is important to understand and revisit assumptions that have been made before. The primary aim of this work is to reconsider and relax a few of these assumptions in theories of dark matter and baryogenesis, exploring alternatives to standard lore.

In chapter 2, we introduce a novel solution to the strong CP problem. We revisit the assumption that the strong CP problem exists everywhere in the universe, and propose a mechanism in which the $\overline{\theta}$ term in QCD can be dynamically cancelled as a result of the local environment of dark matter. In chapter 3, we examine the current-day constraints on a well-studied WIMP DM model, while abandoning the assumption that its abundance today was produced via freezeout in a standard cosmology. Finally, in chapter 4, we explore a novel interplay between the roles of decay and annihilation in generating the baryon asymmetry. Typically, either decay or annihilation dominate the processes that drive the baryon asymmetry. However, we show that both decay and annihilation can operate together, leading to an interesting path to baryogenesis.

Chapter 1

Introduction

Despite the successes of the standard model (SM), many mysteries remain unexplained. For instance, the SM does not contain the field content necessary to explain the dark matter (DM) that fills the universe, why the neutron electric dipole moment (EDM) is measured to be consistent with zero (the strong CP problem), or how the asymmetry between matter and anti-matter arose in the early universe (Baryogenesis). These topics have been the subject of intense study on both the theoretical and experimental fronts.

For many years, particle colliders have been at the forefront of particle physics, due to their ability to directly produce new particles. While this is most certainly still true, using the universe as a laboratory to probe the largest energies will be key to understanding physics beyond the standard model (BSM). The intersection of particle physics and astrophysics and cosmology is becoming ever larger, and it will be important to explore intersections of particle physics and other fields. Understanding and probing BSM physics further will require advances in both theory and experiment, as well as revisiting assumptions made about the regions of parameter space that are interesting. This will be a central theme in this work.

For the remainder of this chapter, we discuss the background necessary for the following chapters. Namely, we broadly discuss some of the general characteristics, models, and detection methods of dark matter, introduce the strong CP problem, the finite temperature potential and phase transitions, and finally we discuss baryogenesis.

1.1 Dark Matter

The identity of dark matter persists as one of the most pressing questions in fundamental physics. Its existence has been cemented by a myriad of astrophysical observations, including galactic rotation curves, the CMB power spectrum, gravitational lensing, and large scale structure formation. Despite its prominent influence on the largest scale structures, its microscopic properties have eluded particle physicists. This is not surprising, however, since the only properties of DM we know are that it is electrically neutral, has mass, and is stable on timescales larger than the age of the universe. Due to this, the space of theories and models is huge.

To motivate where to start looking in this vast space of possibilities, BSM theories that solve other fundamental problems in particle physics often introduce new particles that have the correct features to be dark matter. It is not required that dark matter be necessary to solve any other problems within particle physics or to interact through anything other than gravity, but these motivations give a starting point.

Although DM has not been detected from the particle physics side, the effort to detect DM has provided important constraints on various regions of parameter space. There have been many search strategies for the large variety of DM candidates. A few of the most common search strategies are direct detection, indirect detection, and collider production, for which we discuss below.

Direct Detection: Direct detection searches for the DM by looking for signatures of direct scattering between DM and atoms in a detector. This scattering deposits energy and causes a recoil in the detector, which can be distinguished from the background for some region of the parameter space. To calculate the rates at which this occurs, it is often convenient to work in the language of effective field theory (EFT), due to the low velocities characteristic of galactic DM. Additionally, at these low energies the relevant degrees of freedom are nucleons and we therefore need to map the scattering of the DM with quarks and gluons into DM scattering with nucleons.

We briefly outline how this is done. The interactions that could lead to scattering with nucleons take the form of couplings between DM and quarks and gluons.

$$|\chi|^2\overline{q}q, \qquad |\chi|^2 G^{\mu\nu}G_{\mu\nu} \qquad \text{(Scalar DM)}$$

$$\overline{\chi}\chi\overline{q}q, \qquad \overline{\chi}\gamma^\mu\chi\overline{q}\gamma_\mu q, \qquad \overline{\chi}\gamma^\mu\gamma^5\chi\overline{q}\gamma_\mu\gamma^5 q, \qquad \overline{\chi}\chi G^{\mu\nu}G_{\mu\nu} \qquad \text{(Fermionic DM)}$$

From here, we need to evaluate the matrix element,

$$i\mathcal{M} = \langle\chi(p')\ n(k')|\mathcal{T}\{e^{-i\int H_{\rm int}d^4x}\}|\chi(p)\ n(k)\rangle \tag{1.1}$$

$$\sim \langle\chi(p')\ n(k')|\ i\int d^4x\ \mathcal{L}_{\rm int}\ |\chi(p)\ n(k)\rangle \qquad \text{(To first order)} \tag{1.2}$$

The second line represents the leading order term in our perturbative expansion. The overlap here factorizes into the DM part and the quark/gluon part. For example, the case of the scalar DM coupling schematically gives

$$\mathcal{M} \sim \langle \chi(p')n(k')| \Big(|\chi|^2 \bar{q}q + |\chi|^2 G^{\mu\nu} G_{\mu\nu} \Big) |\chi(p)n(k)\rangle \tag{1.3}$$

$$\sim \langle \chi(p')|\chi\chi|\chi(p)\rangle \langle n(k')|m_q \bar{q}q|n(k)\rangle + \langle \chi(p')|\chi\chi|\chi(p)\rangle \langle n(k')|G_{\mu\nu}G^{\mu\nu}|n(k)\rangle \tag{1.4}$$

where we've dropped the couplings and energy scales for the sake of demonstration. In this case, the quarks and gluons are mapped into the nucleon states by [87]

$$\langle n(k')|m_q \bar{q}q|n(k)\rangle \equiv m_n f^n_{T,q} \bar{u}(k')u(k) \tag{1.5}$$

$$\langle n(k')|\alpha_s G^{\mu\nu} G_{\mu\nu}|n(k)\rangle \equiv -\frac{8\pi}{9} m_n f^n_{T,g} \bar{u}(k')u(k) \ , \tag{1.6}$$

We can then go through the usual process of calculating a scattering cross section once these are evaluated. We will see this again in Ch. 3, where we apply this process to scalar WIMP DM.

Indirect Detection: Indirect detection uses telescopes to search for a flux of photons that is associated with DM annihilation in regions such as the galactic center (GC) and in dwarf spheroidal galaxies (dSphs). Unfortunately, this is subject to astrophysical uncertainties and depending on the source, these uncertainties can be appreciable. For instance, the GC's dark matter density profile is not well known, and the expected signal of photons can vary drastically if the density of DM is cuspy or has a large core.

Additionally, the typical annihilation cross section makes use of the DM interactions occurring at a point, and neglect the possibility of the attraction between two DM particles via a potential generated by a mediator. This long-range attraction enhances the probability that two DM particles could meet at a point to then annihilate. This is referred to as the

Sommerfeld enhancement, and is defined as the ratio of the probabilities of finding the DM meeting at a point under the influence of the potential, versus when there is no potential. This is most relevant in the regime when the DM is non-relativistic, as is the case for galactic DM, and can lead to large enhancements and additional resonant structure.

Collider Production: DM may also be produced in the high energy collisions of particle colliders, which can lead to missing energy signals. There are a plethora of both model dependent and independent search strategies, some of which will be discussed for the WIMP case in Ch.3.

We now turn to reviewing some general classes of DM models.

1.1.1 WIMPs and the WIMP Miracle

Weakly interacting massive particles (WIMPs) make up a general class of DM candidates that have been the focus of DM research for many years. The standard electroweak WIMP's properties are characteristic of electroweak scale particles, which have masses of ~ 100 GeV$-$TeV and electroweak sized couplings. There are a few reasons for their prominence, both on the theoretical and experimental sides. Many BSM theories naturally predict particles near the electroweak scale, which also have the key properties to be dark matter. For example, supersymmetry (SUSY) is a proposed solution to the electroweak hierarchy problem, where an extra symmetry between bosons and fermions is imposed onto the SM which controls the quadratic UV divergences in the corrections to the Higgs mass. This extra symmetry introduces new superpartner particles that arise near the electroweak scale. Some of these superpartner particles, such as the fermionic superpartners to the electroweak and Higgs bosons (i.e. the neutralinos), have the correct characteristics to be dark matter.

To generally characterize WIMP dark matter in a minimal, model independent way, we can

write down general Lagrangians that are governed strictly by their interactions with the electroweak gauge fields. Specific models can add additional interactions on top of this, however, we can cast a wide net over dark matter models by minimally extending the SM to include electroweak WIMPs. This kind of dark matter, known as *Minimal Dark Matter* [47] are described by the Lagrangians,

$$\mathcal{L}_{\text{scalar}} = c\big(|D_\mu \chi|^2 - m_\phi^2 |\chi|^2\big) \tag{1.7}$$

$$\mathcal{L}_{\text{fermion}} = c\overline{\chi}\big(i\not{D} - m_\chi\big)\chi \tag{1.8}$$

depending on whether the WIMP is a scalar or a fermion. Here, $D_\mu = \partial_\mu - i g_W W_\mu^a T^a$ is the gauge covariant derivative, and $c = 1/2$ for a real scalar or Majorana fermion, and $c = 1$ for a complex scalar or Dirac fermion [47]. From these couplings, we can predict the signals that can be produced by a general class of WIMPs. Given the measured density of dark matter, $\rho_{\text{DM}} \sim 0.3$ GeV/cm^3, WIMPs have couplings that are large enough and masses that are small enough to be probed complimentarily by direct detection, indirect detection, and production at colliders. They sit in an ideal spot for detection.

Even further, their attractiveness is also drawn from the evolution of the early universe. Standard lore takes the SM + WIMP dark matter and extrapolates it back to temperatures near the weak scale, assuming a standard cosmology. At these temperatures, the WIMP DM is produced thermally, and its abundance proceeds through the process of thermal freeze-out. The evolution of the DM abundance is governed by the Boltzmann equation,

$$\frac{dn}{dt} + 3Hn = -\langle \sigma v \rangle (n^2 - n_{eq}^2) \tag{1.9}$$

where n is the number density of the DM, H is the Hubble parameter, $\langle \sigma v \rangle$ is the thermally averaged annihilation cross section. Typically the Boltzmann equation must be numerically solved, but general behavior can be gleaned from analytical approximations. The process of thermal freeze-out works as follows: the WIMP is produced in thermal equilibrium with the SM bath at temperatures $T \gg M_{\rm DM}$. As the universe expands and cools below the WIMP mass, the WIMPs continue to annihilate into the SM, but the SM loses its ability to annihilate back into WIMPs. This leads to a departure from thermal equilibrium. Eventually, as the universe expands further and the DM abundance depletes, the DM becomes too dilute to efficiently annihilate anymore, locking in the amount of DM leftover, its so-called relic abundance. More quantitatively, at temperatures below the WIMP mass, $T < M_{\rm DM}$, but while the annihilation of the DM is still efficient, the abundance is Boltzmann suppressed, $n \sim \exp(-M_{\rm DM}/T)$, and one can estimate when the DM will freeze out by comparing the annihilation rate to the expansion rate of the universe. In the limit that the annihilation rate is much faster than the expansion rate, the DM annihilations are able to occur efficiently. In the opposite limit, where the annihilation rate is much slower than the expansion rate, the DM annihilation has effectively turned off. The cross-over between these two limits, i.e. roughly when the annihilation rate is similar to the expansion rate, $n\langle \sigma v \rangle \sim H$, is where the interesting out-of-equilibrium dynamics occurs. This leads to the simple expression that relates the final freeze-out abundance of DM to the temperature and annihilation cross section,

$$n_f \sim \frac{T^2}{M_{\rm pl}\langle \sigma v \rangle} \tag{1.10}$$

To illustrate the scenario for WIMPs, the annihilation cross sections typical of the electroweak WIMP scales as

$$\langle \sigma v \rangle \sim \frac{g_W^4}{M_{\rm WIMP}^2} \tag{1.11}$$

where g_W is the weak coupling strength, $M_{\rm WIMP} \sim 100$ GeV-1 TeV is the typical electroweak WIMP mass. The Boltzmann equation yields a freeze-out abundance of DM that is consistent with the observed density of DM needed to explain astrophysical phenomena [86, 61]. This is referred to as the *WIMP Miracle*.

Despite the attractive picture of the WIMP miracle, there is a growing sense that WIMPs are no longer favored as a candidate to play the role of dark matter. The null results from direct and indirect searches for dark matter in the Galaxy and for its production at colliders have ruled out portions of the parameter space living at the heart of the WIMP miracle. While a large part of this shift in focus is simply driven by the healthy urge to explore a wider parameter space [39] particularly since no concrete observation suggests that the WIMP miracle is realized in nature, it remains important to map out the boundary between what types of WIMP dark matter are allowed, and which are concretely ruled out by null searches. Even in the context of a standard cosmology, WIMP-like dark matter particles whose relic abundance is determined by freeze out remain viable for a range of parameter space (see e.g. [85, 40]).

In chapter 3, we investigate the parameter space of WIMPs that is allowed by null searches, without the assumption of freeze-out in a standard cosmology. We scan through a wide range of masses around the weak scale, $100\,\text{MeV} - 100\,\text{TeV}$, and calculate the constraints over that wide range of masses. Although the production mechanism is an important process to pin down, and standard freeze-out usually fixes the mass to be $\sim$ TeV scale, we proceed by assuming that some cosmology equipped with a production mechanism could lead to a radical change in the mass that would be predicted. Thus, we will derive bounds that will

be robust regardless of the early universe physics that is assumed.

1.1.2 Ultralight Dark Matter

Beyond the WIMP paradigm, there has been much effort in studying models where the DM is ultralight ($m_{\rm DM} \lesssim$ eV). Ultralight DM (ULDM) is necessarily bosonic, due to the large occupation numbers required to accommodate the measured density at these low masses. Fermionic DM would be required to be packed closer in galaxies than the Fermi degeneracy pressure would allow. Fermionic DM's mass can only be as low as a few hundred eV, which is referred to as the Tremaine-Gunn bound [123].

ULDM has also been motivated by problems within the SM. For example, the QCD axion is an ULDM candidate that proposes to solve the strong CP problem. A large class of more general models has undergone intense investigation, such as axion-like particles (ALPs), or other scalar and vector fields.

If the dark matter is an ultralight scalar field ϕ, it acts as a coherent field which oscillates with time $\phi(t) \sim \phi_0 \cos(m_\phi t)$ where $\phi_0 \sim \sqrt{2\rho_{\rm DM}}/m_\phi$. On the other hand, if the dark matter is an ultralight vector, then both its magnitude and spin can oscillate with time. As we will see in Ch. 2, the alignment and magnitude of the spin density of the dark matter can be influenced by external, non-gravitational potentials, governed by the dynamics of the model or theory considered.

ULDM can have masses down to $m_{\rm DM} \sim 10^{-22}$ eV, the so-called *fuzzy limit* [75]. This arises when the de Broglie wavelength of the DM becomes larger than the measured DM halo size of dwarf galaxies. Fuzzy DM was originally proposed to solve a tension between theory and observation about the DM density profile in the galactic halo, where the fuzzy DM smooths cusps at the galactic center into cores.

1.2 The Strong CP Problem

Another problem that the SM does not address is the strong CP problem– a firm tension between theoretical expectations and precision experimental measurements. The theory of the strong interactions is well established as Quantum Chromodynamics, based on an $SU(3)_c$ gauge symmetry with vector-like quarks in the fundamental representation. A wealth of observational data ranging from high energies where the theory is described as weakly coupled quarks and gluons down to low energies where they are confined into color-neutral hadrons has established QCD as an integral building block of the Standard Model (SM).

Despite this unquestionable success, the structure of QCD contains a deep mystery: the symmetries of the theory admit a dimension four interaction term for the gluons which violates CP:

$$\frac{\alpha_s}{8\pi}\ \overline{\theta}\ G_a^{\mu\nu}\widetilde{G}_{\mu\nu}^a \tag{1.12}$$

where $\overline{\theta} \equiv \theta + \text{Arg Det } M_q$ is the basis-independent quantity characterizing the physical combination of the strong phase θ and a phase in the quark Yukawa interactions. Null searches for an electric dipole moment (EDM) of the neutron [104] require $\overline{\theta} \lesssim 10^{-10}$, in contrast to the naive expectation that it be order 1. While it is possible that such a tiny value is simply one of the parameters that Nature has handed us, the extraordinarily minute experimental limit is suggestive that we explore physical explanations.

The most popular explanation invokes a fundamental axion field [127, 126, 82, 115, 56, 130], arising as the pseudo-Nambu Goldstone boson of a spontaneous broken $U(1)_{PQ}$ symmetry

[102, 103] resulting in a coupling of the form

$$\frac{a(x)}{f_a}\, G_a^{\mu\nu}\widetilde{G}^a_{\mu\nu}. \tag{1.13}$$

At low scales, non-perturbative QCD dynamics induce a potential which is schematically of the form $-\Lambda^4 \cos\left(a/f_a - \overline{\theta}\right)$, inducing a vacuum expectation value for a which effectively cancels the net coefficient of the CP-violating term. There is a vibrant experimental program underway to search for axions in various ranges of mass [36].

The basis of the strong CP problem relies on the measurement of the EDM of the neutron, which was measured here on Earth. However, the axion solution provides a mechanism for dynamically cancelling the neutron EDM globally. Although elegant, we do not need to solve the problem globally, since we only know it exists locally. That is, the neutron may not have a vanishing EDM elsewhere in the universe. With this in mind, we consider an alternative solution to the axion, one which solves the strong CP problem by canceling the neutron EDM near the Earth via environmental effects, where the dark matter in the galactic halo has spin dependent interactions that are governed by their couplings to gluons.

The general solution looks similar to that of the axion solution, i.e. we add some coupling of the dark matter to $G\widetilde{G}$. The spin of the dark matter is the degree of freedom that plays the significant role of cancelling $\overline{\theta}$. The dark matter's other degree of freedom, its mass density, is already governed by the external gravitational potential of the galaxy. We therefore consider interactions of the form:

$$\mathcal{L}_{\text{DM}-\text{Gluon}} = \sum_i \frac{1}{M_*^i}\mathcal{O}_i^S G\widetilde{G} \tag{1.14}$$

where $\mathcal{O}_i^S$ is an operator of dimension i that incorporates the spin of the dark matter, and M_* is the energy scale of the UV dynamics encoded in the EFT. This operator should cause the spins to align in a direction chosen by the QCD potential, such that when the dark matter is coherently aligned on large length scales, it dynamically cancels $\overline{\theta}$.

In chapter 2, we investigate one such solution where the dark matter is a massive vector, necessitated by the need for a spin degree of freedom as well as it generically needing to be ultra-light. We build the operator including the spins of the vector DM, $\mathcal{O}_i^S$, by finding the Noether current associated with rotations. To separate out the spin from the orbital angular momentum, we then take the position independent portion of this current. We then explore some of the phenomenological consequences of such a model.

1.3 Finite Temperature Potential and Phase Transitions

We move on to discussing the formalism for calculating finite temperature corrections to the tree-level potential. Taking these effects into account illuminates the possibility of a change of vacuum phase in the early universe. These cosmological phase transitions represent a dramatic change in the properties of the Universe over a relatively short period of its history, and may play an important role in our understanding of conditions today. Already in the Standard Model (SM), the QCD phase transition at which $SU(3)$ color confines [101] is thought to separate a phase dominated by free quarks and gluons from one where the relevant degrees of freedom are baryons, and the electroweak (EW) phase transition demarcates a period where the electroweak gauge symmetry is exact from one in which the weak bosons and SM fermions have non-zero masses. In the context of physics beyond the Standard Model (BSM), first order phase transitions (FOPTs) are frequently invoked to catalyze interesting

dynamics. We review some of the aspects of phase transitions.

We begin by writing down the tree-level potential for a new complex scalar, Φ, which is a SM singlet.

$$V(\Phi) = -\mu_\phi^2 \Phi^* \Phi + \frac{\lambda_\phi}{4}(\Phi^* \Phi)^2 \tag{1.15}$$

We can expand Φ as

$$\Phi = \frac{1}{\sqrt{2}}(v + \phi)e^{-ia/v} \tag{1.16}$$

where ϕ is a real scalar field, and a is the Nambu-Goldstone boson. Quantum corrections to the scalar potential yield important effects, and leads to complex dynamics. We can calculate the Coleman-Weinberg effective potential and the finite temperature corrections to the potential at one loop, via tadpole diagrams [114].

The one-loop scalar effective potential including finite temperature effects is given by:

$$\begin{aligned} V_{\text{eff}}(T) = &-\frac{1}{2}\mu_\phi^2 \phi^2 + \frac{1}{4}\lambda_\phi \phi^4 \\ &+ V_{\text{CW}}(\phi) \\ &+ \frac{T^4}{2\pi^2}\sum_i (-1)^F n_i J_{B/F}\left(\frac{m_i^2}{T^2}\right) \end{aligned} \tag{1.17}$$

where n_i is the number of spin degrees of freedom for each species of field within the loop.

Here, the Coleman-Weinberg potential $V_{\rm CW}(\phi)$ is

$$V_{\rm CW}(\phi) = \begin{cases} \frac{1}{64\pi^2} m_s(\phi)^4 \phi^4 \left(\log\left(\frac{m_s(\phi)^2}{\Lambda^2}\right) - \frac{3}{2} \right) & \text{Scalars} \\ -\frac{n_F}{64\pi^2} m_F(\phi)^4 \left(\log\left(\frac{m_F(\phi)^2}{\Lambda^2}\right) - \frac{3}{2} \right) & \text{Fermions} \\ \frac{3}{64\pi^2} m_V(\phi)^4 \left(\log\left(\frac{m_V(\phi)^2}{\Lambda^2}\right) - \frac{3}{2} \right) & \text{Vectors} \end{cases} \tag{1.18}$$

where $m_i(\phi)$ is the ϕ-dependent mass of the fields running in the loops, $n_F = 2$ for Majorana fermions, $n_F = 4$ for Dirac fermions, and the thermal functions $J_{B/F}(m_i^2/T^2)$ are given by

$$J_{B/F}(x) = \int_0^\infty dy\ y^2 \ln\left(1 - (-1)^F e^{\left(-\sqrt{y^2+x}\right)}\right) \tag{1.19}$$

In the high temperature limit, $J_{B/F}(m_i^2/T^2)$ can be expanded as,

$$J_B\left(\frac{m_i^2}{T^2}\right) = -\frac{\pi^4}{45} + \frac{\pi^2}{12}\frac{m_i^2}{T^2} - \frac{\pi}{6}\left(\frac{m_i^2}{T^2}\right)^{3/2} - \frac{1}{32}\frac{m_i^4}{T^4}\log\left(\frac{m_i^2}{16\alpha T^2}\right) + \mathcal{O}\left(\frac{m_i^6}{T^6}\right) \tag{1.20}$$

$$J_F\left(\frac{m_i^2}{T^2}\right) = \frac{7\pi^4}{360} - \frac{\pi^2}{24}\frac{m_i^2}{T^2} - \frac{1}{32}\frac{m_i^4}{T^4}\log\left(\frac{m_i^2}{16\alpha T^2}\right) + \mathcal{O}\left(\frac{m_i^6}{T^6}\right)$$

At large T, the finite temperature term dominates, with only one vacuum available for the scalar to occupy. As the temperature decreases, a second vacuum emerges, and eventually becomes energetically favorable after the critical temperature is reached. The introduction of bosonic fields generate a cubic term that comes from the high temperature expansion of

the thermal functions. This generates a barrier between the two minima, and the phase transition can be first order. Rewriting the finite temperature potential as,

$$V(\phi, T) = D(T^2 - T_0^2)\phi^2 - ET\phi^3 + \frac{\lambda(T)}{4}\phi^4 \tag{1.21}$$

where D, E, and $\lambda(T)$ are determined via the effective potential and high temperature expansion of the thermal functions. From these parameters, we can calculate the critical temperature, T_c, nucleation temperature, T_n, and the strength of the phase transition. In terms of these parameters, the critical temperature is given by:

$$T_c = \frac{T_0\sqrt{\lambda(T_c)D}}{\sqrt{\lambda(T_c)D - E^2}} \tag{1.22}$$

To first approximation, we can determine the strength of the FOPT, by taking the ratio $\langle\phi\rangle|_{T=T_n}/T_n$. However, T_n will be determined numerically, so it is useful to look at the analytic approximation,

$$\frac{\langle\phi\rangle|_{T=T_c}}{T_c} \sim \frac{E}{\lambda(T_c)} \gg 1 \quad \text{for strong FOPT} \tag{1.23}$$

which serves as a check for the more precise measure of the strength of phase transition. Since $T_c > T_n$ and $\langle\phi\rangle|_{T=T_c} < \langle\phi\rangle|_{T=T_n}$, if this estimate suggests a strongly first-order phase transition, so will $\langle\phi\rangle|_{T=T_n}/T_n$.

We can determine the nucleation temperature by requiring the rate of nucleation be equal

to the Hubble rate [128],

$$\Gamma_{\text{tunnel}}/H \sim \frac{M_{pl}^4 T_n^4}{\rho^2} e^{-S_3/T_n} \tag{1.24}$$

$$\sim \frac{M_{pl}^4}{T^4} e^{-S_3/T_n} \geq 1 \tag{1.25}$$

A semi-analytic solution exists for the three-dimensional Euclidean action, which must be determined to calculate the nucleation rate [9, 81]. This yields the condition,

$$\frac{S_3}{T_n} \simeq \frac{64\sqrt{2}\pi}{81} \frac{E}{\lambda(T_n)^{3/2}} (2-\delta)^{-2} (\beta_1 \delta + \beta_2 \delta^2 + \beta_3 \delta^3) \approx A \tag{1.26}$$

where $A \approx 142$ for temperatures near the electroweak scale, and is determined by Eq. 1.25, $\delta = \lambda_\phi D(T^2 - T^0)/2(ET)^2$ and $\beta_1 = 8.2983,\ \beta_2 = -5.5330$, and $\beta_3 = 0.8180$ [9, 91]. We are then able to approximate the nucleation temperature and rate.

1.4 Baryogenesis

The origin of the asymmetry between matter and antimatter is yet another outstanding problem in particle physics and cosmology. The SM alone fails to be able to generate the asymmetry observed, which can be parameterized by the baryon to photon ratio, $\eta_b = n_b/n_\gamma = 6.2 \times 10^{-10}$. Thus, mechanisms beyond the standard model must be considered. For any mechanism to yield successful baryogenesis, it must satisfy the three Sakharov conditions [111]. That is, a mechanism must satisfy

1. Baryon number violation

2. C and CP violation

3. Departure from thermal equilibrium

Popular models have included electroweak baryogenesis (EWBG) [43, 49, 84] and leptogenesis [55]. EWBG modifies the SM to generate a first-order electroweak phase transition which produces a separation of phases in which the electroweak sphalerons are active and inactive. The baryon asymmetry generated by these sphalerons can be locked in without being washed-out in the broken phase. Leptogenesis introduces heavy right-handed neutrinos whose CP violating decays generate an asymmetry in the lepton sector. This lepton asymmetry is then converted into a baryon asymmetry via the electroweak sphalerons.

In chapter 4, we explore a radically different scenario, where a first order phase transition is responsible for changing the relationship between decays and annihilation, by way of interactions between new particles and the bubble walls. Due to annihilation processes having different diagram topologies, the CP violation from annihilation can be different and larger than that of the decays, leading to the production of the asymmetry with different requirements. Thus, the interplay between decay and annihilation in this scenario can provide an interesting route to baryogenesis.

Chapter 2

An Emergent Solution to the Strong CP Problem

This chapter heavily relies on previously published work in collaboration with Arvind Rajaraman and Tim M.P Tait [19]

In this chapter, we propose a new class of solution to the strong CP problem. We consider a theory in which there is no fundamental axion field, but in which the dark matter, necessary to explain cosmological observations, is composed of light vector particles which couple to the gluons in such a way that the net local spin density acts in some ways like an emergent degree of freedom which cancels $\overline{\theta}$. The axion can be understood as an emergent phenomenon, similar in character to the spin-wave excitations observed in condensed matter systems.

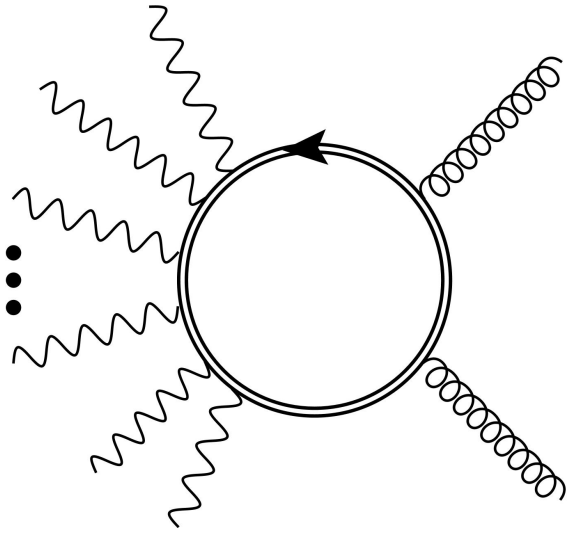

Figure 2.1: Representative Feynman diagram indicating how integrating out $\mathrm{SU}(3)_c$-charged fermions can generate an interaction between the dark matter and gluons.

2.1 Dark Matter

The dark matter is assumed to be a massive vector A_μ described by the free Lagrangian,

$$\mathcal{L} = -\frac{1}{4} F_{\mu\nu} F^{\mu\nu} + \frac{1}{2} m^2 A_\mu A^\mu \tag{2.1}$$

where $F_{\mu\nu} \equiv \partial_\mu A_\nu - \partial_\nu A_\mu$ is the usual field strength tensor, and m can be understood as either a Stückelberg mass or as arising from a dark Higgs sector. We introduce an interaction between the dark matter and the SM gluons through operators of the form,

$$\frac{\alpha_s}{16\pi} \frac{1}{M_*^{(6+2n)}} \; S^{\mu\nu\rho} S_{\mu\nu\rho} \left(A^\alpha A_\alpha\right)^n \; G^a_{\sigma\lambda} \widetilde{G}^{\sigma\lambda}_a \tag{2.2}$$

where

$$S^{\mu\nu\rho}[A] \equiv F^{\mu\nu}A^{\rho} - F^{\mu\rho}A^{\nu} \tag{2.3}$$

is the functional of A_μ representing the position-independent portion of the Noether current corresponding to rotations, and thus corresponds in the non-relativistic limit to the net spin density carried by the A_μ field, $\vec{S}_i \sim \epsilon_{ijk}S^{0jk}$. M_* characterizes the strength of the interaction and has units of energy, and n is an integer. Such interactions could be generated, for example, by integrating out heavy $\mathrm{SU}(3)_c$-charged degrees of freedom which couple to the dark matter (see Figure 2.1). In that case, one would expect the low energy theory to contain the whole family of operators for all values of n.

The interaction, Eq. (2.2) is not manifestly gauge invariant, and can be understood to be written in the unitary gauge. As dictated by dark gauge-invariance, the dependence of M_* on the underlying UV parameters depends on the form of the UV theory. For example, if the $\mathrm{SU}(3)_c$-charged fermions in the loop are chiral, and get their mass from the same dark Higgs vacuum expectation value v_D which breaks the dark gauge symmetry, one would expect the coefficient of the interaction to get a contribution at 1-loop of the form $\int d^4k\, k^4\, m_\Psi^{(2+2n)}/(k^2 - m^2)^{(6+2n)} \sim \partial^4/M_*^{6+2n}$, where $m_\Psi = yv_D$ is the mass generated by the Yukawa interaction, and the vector fields A_μ would be longitudinal modes arising from the would-be Goldstone bosons. Note that the loop integral goes to zero when v_D goes to zero, as expected from gauge invariance.

This operator allows collisions at high energy colliders to produce (multi-particle) dark matter states, and is bounded by searches for mono-jets recoiling against missing momentum [63, 28]. While detailed analyses for this specific interaction do not exist, existing mono-jet searches are expected to require $M_* \gtrsim$ a few hundred GeV [1].

2.2 Effective Local Theta

As we will see below, the necessary masses for the dark matter are very small, and we assume that the local dark matter in the galactic halo can be described as a coherent state characterized by its expectation values of energy and the quantity $\langle S^{0ij} S_{0ij} A^{2n} \rangle$ contained in the interaction Eq. (2.2). These two quantities are simultaneously measurable, as can be demonstrated by observing that the Hamiltonian density $\mathcal{H} \equiv T^{00}$ is the 00 component of the energy momentum tensor, which in the noninteracting limit takes the form $T^{\mu\nu} = F^{\mu\alpha}F^{\nu}_{\alpha} + \frac{1}{4}\eta^{\mu\nu}F^{\rho\sigma}F_{\rho\sigma} + m^2(A^{\mu}A^{\nu} - \frac{1}{2}\eta^{\mu\nu}A^{\rho}A_{\rho})$, and satisfies $[S^{0ij}, \mathcal{H}] = 0$. In the non-relativistic limit, $\mathcal{H}$ reduces to m^2A^2, such that $S^{0ij}S_{0ij}\mathcal{H}^n/m^{2n} \to S^{0ij}S_{0ij}A^{2n}$.

The dynamics of the dark matter in a region of space close to the solar location is described by a partition function with the UV dynamics of QCD encoded (schematically) by a short distance potential and the long distance influence of the gravitational dynamics of the galaxy represented by an external potential:

$$-\Lambda^4 \cos\left(\frac{S^{\mu\nu\rho}S_{\mu\nu\rho}\left(A^2\right)^n}{M_*^{(6+2n)}} - \overline{\theta}\right) - \mu\ T^{00}, \tag{2.4}$$

with μ adjusted such that it enforces the local energy density consistent with the Galactic gravitational dynamics,

$$\langle T^{00} \rangle = \rho_{\odot} \sim 0.3\ \mathrm{GeV/cm^3} \sim 3 \times 10^{-7}\ \mathrm{eV}^4. \tag{2.5}$$

In a particular region of space, the contribution from the dark matter to the effective θ-term is bounded by the maximum spin density consistent with the local number density of

the dark matter. In terms of the amplitude of the coherent state $\mathcal{A}$, the derivatives scale as $\langle \partial_0 A \rangle \sim m\mathcal{A}$, $\langle \partial_i A \rangle \sim mv\mathcal{A}$ (where $v \sim 10^{-3}$ is the typical velocity dispersion), and $\langle S^{0ij} \rangle \sim sm\mathcal{A}^2$, where $0 \leq s \leq 1$ characterizes the degree to which the field is polarized. In this language, the long distance contribution to the effective potential determines $\mathcal{A}$, and the QCD contribution acts to prefer a local value of s which minimizes the effective θ term in that region of space.

The dark matter contribution to the effective θ is parametrically,

$$\frac{s^2 m^2 \mathcal{A}^{(4+2n)}}{M_*^{(6+2n)}} \sim s^2 \frac{\rho^{(2+n)}}{M_*^{(6+2n)} m^{(2+2n)}}. \tag{2.6}$$

In order to cancel a $\overline{\theta}$ of order one near the Sun, the mass of the dark matter must satisfy,

$$m \lesssim \left(\frac{\rho_\odot^{(2+n)}}{M_*^{(6+2n)}} \right)^{\frac{1}{2+2n}}. \tag{2.7}$$

The maximum m as a function of the operator dimension n is plotted for $M_* = 1$ TeV in Figure 2.2. For $n \geq 3$, masses large enough to be consistent with the bound on the fuzziness of dark matter on small scales [33, 92, 98, 97] are consistent with the emergent solution to the strong CP problem.

While operators containing larger values of n are necessary to consistently cancel $\overline{\theta}$ near the Earth, it is clear that the (unavoidable) presence of operators with lower n are not problematic. Given the local density of dark matter, the lower n operators make a negligible contribution to the local effective θ term. Operators with higher n occur at the same order in the loop expansion, though they are suppressed by additional powers of M_*.

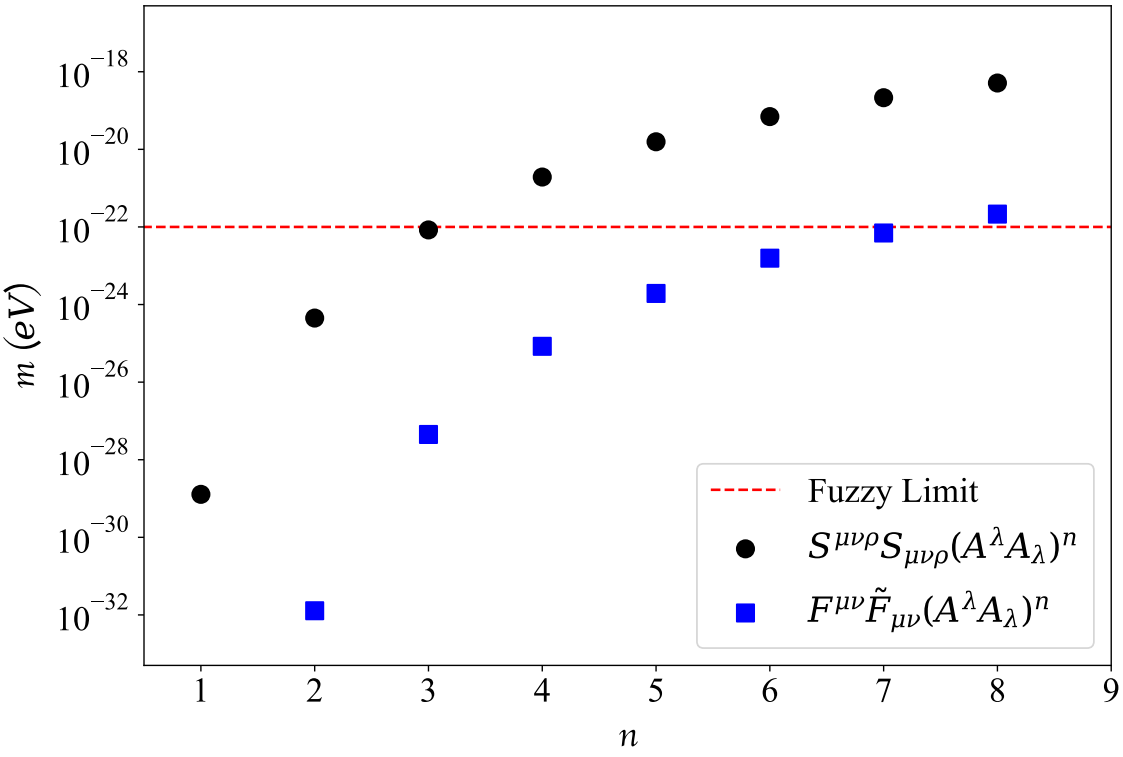

Figure 2.2: Maximum dark matter mass consistent with solving the strong CP problem near the Earth, as a function of the operator dimension n (black circles). The red dashed line indicates the bound on the dark matter mass from small scale structure [33, 92, 98]. The blue squares indicate the maximum masses from the alternative interaction, Eq. (2.19).

2.2.1 Additional Contributions to θ_{eff}

Our analysis so far has assumed that the QCD potential represents the only important dynamics influencing the dark matter spin density. It is crucial that any other contributions be sufficiently subdominant that they deflect s from the minimum of Equation (2.4) such that the effective θ term remains $\lesssim 10^{-10}$.

The same dynamics which gives rise to the operator connecting the dark matter to $G\widetilde{G}$ will also lead to operators containing dependence on s which is unaligned with $\overline{\theta}$. These operators

take the form,

$$\frac{a_p}{16\pi^2}\frac{1}{M_*^{(8+2p)}}\left(S^{\mu\nu\rho}S_{\mu\nu\rho}\right)^2\left(A_\lambda A^\lambda\right)^p \tag{2.8}$$

where p is an integer which characterizes the operator making the dominant contribution, and a_p is a dimensionless coefficient which could be computed given a more concretely realized UV theory. This operator will shift s from the minimum cancelling $\overline{\theta}$, inducing an effective θ term of order:

$$\delta\theta \;\sim\; \frac{\rho_\odot^2}{\Lambda^4 m^2 M_*^2}\times\left(\frac{\rho_\odot}{m^2M_*^2}\right)^{p-n}. \tag{2.9}$$

For $m\sim 10^{-18}$ eV and $M_*\sim 1$ TeV, the effective local θ term is acceptably small provided $p\lesssim n+5$.

The local environment may also impose a preference on the net dark matter spin density. For example, the dark matter may possess a magnetic dipole moment, described by e.g.,

$$\frac{e\lambda_m}{16\pi^2M_*^4}F_{\rm EM}^{\mu\nu}\;\partial^2\left(F_{\nu\rho}\right)\;F_\mu^\rho \tag{2.10}$$

where $F_{\rm EM}$ is the electromagnetic field strength, e is the electric coupling, and λ_m is a dimensionless quantity. If the mediator fermions carry electroweak charge, one would expect the magnetic dipole is induced at one loop, and $\lambda_m\sim 1$, whereas if not it will nonetheless be induced at three loops, $\lambda_m\sim(\alpha_S(M_*)/4\pi)^2$. At the surface of the Earth, this induces a

shift in the effective theta term of order,

$$\delta\theta \sim \frac{e\lambda_m}{32\pi^2}\frac{B_\oplus m^{(3+n)} M_*^{(-1+n)}}{\Lambda^4 \rho_\odot^{n/2}} \tag{2.11}$$

where $B_\oplus \sim 3 \times 10^{-3}$ eV^2 is the strength of the Earth's magnetic field at its surface. Even for $\lambda_m \sim 1$, this is far too small to be important for the masses of interest.

If the dark matter interacts directly with electrons with coupling g_D (e.g. through a small amount of kinetic mixing with the hypercharge interaction), it will typically induce a magnetic moment that is larger by $\lambda_m \sim g_D^2 M_*^2/m_e^2$, where m_e is the mass of the electron. Even for order one coupling strengths $g_D \sim 1$, this is small enough as to not significantly destabilize the local effective value of θ.

Even in the absence of a magnetic moment, there is a gravitational interaction between the dark matter spin and the spin of the Earth. These corrections are encapsulated by the potential on the net dark matter spin density induced by the Earth's gravitational field, described as a background Kerr metric characterized by its Schwarzschild radius $r_s = 2GM_\oplus \sim 10^5$ eV^{-1} and angular momentum per unit mass $\vec{a} = \vec{J}_\oplus/M_\oplus$; $|\vec{a}| \sim 10^5$ eV^{-1}. To linear order in r_s and $\vec{a}$, the term in the effective Lagrangian at a position $\vec{r}$ from the center of the Earth reads,

$$\frac{r_s m}{2r^3}(\vec{r}\times\vec{a})\cdot\{(\vec{A}\times\vec{\partial})\times\vec{A}\} + \frac{r_s m^2}{r^3}A_0\ \vec{a}\cdot(\vec{r}\times\vec{A}). \tag{2.12}$$

The correction to the local value of the effective θ is,

$$\frac{r_s|\vec{a}|v}{R_\oplus^2}\frac{M_*^{3+n} m^{1+n}}{\Lambda^4\rho_\odot^{n/2}}, \tag{2.13}$$

where $R_\oplus$ is the radius of the Earth. For the parameters of interest, this is negligibly small.

2.3 Phenomenology

2.3.1 Cosmological Production

As with any ultralight boson playing the role of dark matter, it is necessary to invoke a non-thermal production mechanism which results in a non-relativistic momentum distribution. For the low masses of interest here, production through inflationary fluctuations is thought to be inefficient given the current upper bound on the inflationary scale [99, 22, 65]. Production through a generic tachyonic instability is possible, though it requires some fine-tuning [48, 35, 11]. Masses as low as $\sim 10^{-18}$ eV can be accommodated if the vector mass results from a dark Higgs whose mass is close to the dark matter mass [57].

2.3.2 Structure of Galaxies

For masses close to the fuzzy limit, small scale structures are prevented from forming, and the cusps of large galaxies are typically smoothed into cores [75, 77]. For masses on the larger end of the range we consider, these effects are unlikely to be observable.

A potentially important feature stems from the fact that dense areas of dark matter have a smaller effective θ, and thus a lower vacuum energy. If one treats the background of dark energy as a cosmological constant, and tunes its value such that in regions with very little dark matter, the net vacuum energy reproduces the observed acceleration of the cosmological expansion, this implies that regions containing over-densities of dark matter experience a net negative contribution to their vacuum energy from QCD. This feature could lead to interesting modifications to the usual cosmology and history of structure formation (e.g.

[67]). However, at face value this picture implies a dramatic modification to the dynamics of galaxies, and may pose a serious challenge unless there is some mechanism which operates locally to cancel contributions to dark energy (perhaps as a solution to the cosmological constant problem).

A less dramatic solution would be to invoke $n \gtrsim 6$ and dark matter masses closer to the fuzzy limit, for which the cosmological density of dark matter is sufficient to solve the strong CP problem across the entire Universe. In that case, one adjusts the cosmological constant such that it leads to the observed cosmological acceleration, without any particular impact on galactic dynamics.

2.3.3 Signals at Gravitational Wave Detectors

The mechanism by which the vector dark matter environmentally solves the strong CP problem is somewhat agnostic as to its interactions with the Standard Model fermions. There could be a small direct coupling, or one could be induced through kinetic mixing with the ordinary photon. In that case, the motion of the Earth through the dark matter halo induces an additional time-dependent contribution to the force between objects at a tiny level which is nonetheless accessible to interferometers designed to detect gravitational waves [106]. In the mass range of interest, the current best constraints from the Eöt-Wash experiment [122, 113] require the coupling to ordinary matter be less than about $e \times 10^{-23}$, depending on the details of which SM fermions interact with the light boson, and the LISA experiment is expected to eventually improve on these limits for masses $\gtrsim 10^{-18}$ eV [106].

2.3.4 Distant CP Violation

Any environmental solution to the strong CP problem based on the background of dark matter can have an important consequence: regions without dark matter may be unable to completely cancel the effective θ, and thus have different microscopic physics compared with the solar system, characterized by the protons and neutrons in those regions of space possessing large electric dipole moments whose magnitude corresponds to the local value of θ_{eff} and can be estimated from chiral perturbation theory [121, 94],

$$d_p \simeq \frac{e g_A c_+ \tilde{m}\ \theta_{\text{eff}}}{8\pi^2 f_\pi^2} \log\left(\frac{\Lambda^2}{m_\pi^2}\right), \tag{2.14}$$

where the axial coupling $g_A \sim 1.27$ and $c_+ \sim 1.7$ are terms in the chiral Lagrangian, and $\tilde{m} \equiv m_u m_d/(m_u + m_d) \sim 1.2$ MeV is the reduced quark mass. In regions with θ_{eff} of order one, d_p is of order $10^{-16} e$ cm. This large CP violation is unlikely to lead to large changes in stellar dynamics and evolution [124], but could potentially lead to observable deviations in the atomic physics of stars in regions with lower dark matter density, such as in the outskirts of the Milky Way, or in nearby globular clusters.

Since the bulk composition of stars is hydrogen, we examine the impact of a proton electric dipole moment on its atomic transitions. Treating the electric dipole as a perturbation, the first order correction to the nlm electronic wave function of a hydrogen atom, $|\delta\Psi_{nlm}\rangle$, is given by,

$$|\delta\Psi_{nlm}\rangle = \sum_{(n'l'm')} \frac{\langle\Psi_{n'l'm'}|\hat{H}'|\Psi_{nlm}\rangle}{E_{nlm} - E_{n'l'm'}} |\Psi_{n'l'm'}\rangle \tag{2.15}$$

where $\hat{H}'$ is the additional electric dipole field induced by the proton at the origin, and E_{nlm} and $|\Psi_{nlm}\rangle$ are the unperturbed energy level and unperturbed state vector of the nlm state.

The dipole interaction induces mixing between the unperturbed $l = 0$ and $l = 1$ states, which allows for E1 single photon $2s \to 1s$ transitions through the correction to $|\delta\Psi_{200}\rangle$ proportional to $|\Psi_{n'10}\rangle$:

$$\langle\Psi_{n'10}|\delta\Psi_{200}\rangle = \frac{d_p\ e}{4\pi\sqrt{3}\epsilon_0}\frac{C_{n'1}C_{20}}{E_{n'10} - E_{200}} \times \int_0^\infty dr\ e^{-\frac{r}{a_0}(\frac{1}{n'}+\frac{1}{2})}\frac{2r}{n'a_0}L^3_{n'-2}\left(\frac{2r}{n'a_0}\right)L^1_1\left(\frac{r}{a_0}\right) \tag{2.16}$$

where C_{nl} are the hydrogen wave function normalization coefficients, a_0 is the Bohr radius, $L^l_n(x)$ are the associated Laguerre polynomials, and the z axis has been chosen along the direction of the electric dipole.

The rate for E1 emission of a single photon via the transition from the $2s$ to the $1s$ state is [112],

$$\Gamma(2s \to 1s + \gamma) = \frac{e^2\omega^3}{3\pi}|\langle\Psi_{100}|\ \hat{r}\ |\delta\Psi_{200}\rangle|^2 \tag{2.17}$$

$$\simeq 10^{-24}\ \text{eV} \times \theta^2_{\text{eff}}, \tag{2.18}$$

where $\hat{r}$ is the position operator and $\omega \equiv E_{200} - E_{100}$. In regions where θ_{eff} is of order unity, this represents an enhancement of the rate for this transition by a factor of about 10^4 compared with the CP-conserving M1 transition [96]. In principle, a powerful telescope collecting spectroscopic information could potentially discern this transition line and infer its rate. Resolving this transition from the nearby CP-conserving $2p \to 1s$ line would require a wavelength resolution of order $\delta\lambda/\lambda \sim 10^6$, which is about an order of magnitude beyond the current capabilities of an instrument such as the Keck telescope [125].

2.4 Conclusions and Outlook

We have explored a novel solution to the strong CP problem based on the dark matter environment. The dark matter is an ultralight light vector particle with mass $\lesssim 10^{-18}$ eV, whose spin density is coupled to the gluon field in such a way as to allow it to cancel an order one $\overline{\theta}$ at the position of the Earth. Regions with sufficiently small densities of dark matter cannot locally cancel an order one $\overline{\theta}$, perhaps leading to areas of the Universe in which CP is not locally conserved, and potentially a novel history for structure formation.

We have explored a particular operator, Eq. (2.2), in which the dark matter spin is coupled to the gluon $G\widetilde{G}$. There are a wider array of possible operators, as any operator involving the dark matter spin (and enhanced by its number density) could potentially work. For example, the operator,

$$\frac{\alpha_s}{16\pi}\frac{1}{M_*^{(4+2n)}}\ F^{\mu\nu}\widetilde{F}_{\mu\nu}\left(A^\lambda A_\lambda\right)^n\ G^a_{\sigma\lambda}\widetilde{G}_a^{\sigma\lambda} \tag{2.19}$$

is less suppressed by the interaction scale M_*, though additionally suppressed from the spatial derivatives of the dark matter field. From Figure 2.2, we see that slightly lower masses for the dark matter, though nonetheless consistent with the fuzzy limits for $n \gtrsim 7$, are required to cancel an order one $\overline{\theta}$ at the position of the Earth. This operator has the additional complication that $F\widetilde{F}A^{2n}$ does not commute with the Hamiltonian, implying an intrinsically quantum mechanical dynamic for the evolution of the Galaxy. We leave more detailed thought concerning this interesting possibility for future work.

Chapter 3

Is a Miracle-less WIMP Ruled Out?

This chapter heavily relies on previously published work in collaboration with Tim M.P Tait [21]

In this chapter, we explore the viability of a dark matter particle with standard electroweak interactions, but whose relic abundance is not set by freeze out during a standard cosmology. Given the lack of solid observational probes at times before Big Bang Nucleosynthesis (BBN), which itself occurs long after a typical WIMP would have frozen out, it is not difficult to imagine modifications to the standard cosmology which are consistent with observations, but yield a radically different picture of the parameter space favored by its abundance [62, 69, 38, 34]. We focus on the simple representative case of dark matter described by a real scalar field transforming as a triplet under the $\mathrm{SU}(2)_{\mathrm{EW}}$ interaction of the Standard Model. This construction was previously considered as a specific case of "Minimal Dark Matter" in Ref. [47] and (aside from spin) is similar to the limit of the Minimal Supersymmetric Standard Model in which the wino is much lighter than the other super-partners. With some assumptions, such a particle realizes the WIMP miracle for a mass around 2 TeV [47].

We proceed by assuming that the correct relic abundance for any mass could in principle be realized by suitable modification of the cosmological history (without diving into the specific details as to how this occurs), and examine the observational constraints on the parameter space based on existing null searches for dark matter.

This chapter is organized as follows: Section 3.1 describes the theoretical framework, including the full set of renormalizable interactions, and the leading higher dimensional operators which lead to splitting of the masses of the states within the electroweak multiplet. Section 3.2 reviews constraints from high energy accelerators, and Section 3.3 those from direct searches for the dark matter scattering with terrestrial targets. Section 3.4 examines the important bounds from indirect searches for dark matter annihilation. We reserve Section 4.5 for our conclusions.

3.1 Spin Zero SU(2)-Triplet Dark Matter

Our low energy effective theory contains the entire Standard Model plus a real $\mathrm{SU}(2)_{\mathrm{EW}}$ triplet scalar field ϕ with zero hyper-charge. We impose an exact $\mathbb{Z}_2$ discrete symmetry under which the dark matter transforms as $\phi \to -\phi$, and the SM fields are all even, to forbid interactions that could lead to the dark matter decaying into purely SM final states. The most general, renormalizable Lagrangian consistent with these symmetries is:

$$\mathcal{L}_{\mathrm{DM}} = \frac{1}{2}(D_\mu \phi)_i (D^\mu \phi)_i - \frac{1}{2}\mu_\phi^2 \phi^2 - \frac{1}{4!}\lambda_\phi \phi^4 - \lambda H^\dagger H \phi^2 \tag{3.1}$$

where H is the SM Higgs doublet, and $D_\mu \equiv \partial_\mu - i g_w W_\mu^a T^a$ is the gauge covariant derivative with T_ϕ^a the generators of $\mathrm{SU}(2)_{\mathrm{EW}}$ in the triplet representation. The quartic terms whose strengths are parameterized by λ_ϕ and λ characterize the dark matter self-interactions, and an additional connection to the Standard Model via the Higgs portal [41]. Without the $\mathbb{Z}_2$

symmetry, the the term $H^\dagger \phi H$ would be allowed, and would mediate decays through pairs of SM Higgs/Goldstone bosons[1].

The triplet ϕ contains a pair of charged fields $\phi^\pm$ and a neutral field ϕ^0 which plays the role of dark matter. Expanding both ϕ and the SM Higgs doublet in components (in the unitary gauge), the Lagrangian density, Eq. (3.1) reads,

$$\begin{aligned}
\mathcal{L}_{\rm DM} = \; & \partial_\mu \phi^+ \partial^\mu \phi^- + \frac{1}{2}\partial_\mu \phi^0 \partial^\mu \phi^0 - \frac{\mu_\phi^2}{2}(\phi^0)^2 - \mu_\phi^2 \phi^+ \phi^- \\
& + i g_2 \Big(W_\mu^- (\phi^+ \partial^\mu \phi^0 - \phi^0 \partial^\mu \phi^+) + W_\mu^+ (\phi^0 \partial^\mu \phi^- - \phi^- \partial^\mu \phi^0) \\
& \qquad + (A_\mu \sin\theta_W + Z_\mu \cos\theta_W)(\phi^+ \partial^\mu \phi^- + \phi^- \partial^\mu \phi^+) \Big) \\
& + g_2^2 \Big(W_\mu^+ W^{-\mu} \phi^0 \phi^0 + 2 W_\mu^+ W^{-\mu} \phi^+ \phi^- - W_\mu^+ W^{+\mu} \phi^- \phi^- - W_\mu^- W^{-\mu} \phi^+ \phi^+ \\
& \qquad + (A_\mu A^\mu \sin^2\theta_W + 2 A_\mu Z^\mu \sin\theta_W \cos\theta_W + Z_\mu Z^\mu \cos^2\theta_W)(\phi^- \phi^+) \\
& \qquad - (W_\mu^+ \phi^- \phi^0 + W_\mu^- \phi^+ \phi^0)(A^\mu \sin\theta_W + Z^\mu \cos\theta_W) \Big) \\
& - \lambda \left(\frac{1}{4} v^2 (\phi^0)^2 + \frac{1}{2} v h (\phi^0)^2 + \frac{1}{4}(\phi^0)^2 h^2 + \frac{1}{2} v^2 \phi^+ \phi^- + v h \phi^+ \phi^- + \frac{1}{2}(\phi^+ \phi^-) h^2 \right) .
\end{aligned} \tag{3.2}$$

The interactions with the Standard Model are via the electroweak gauge bosons, whose couplings are controlled by e and $\sin\theta_W$, and take the familiar form dictated by gauge invariance. The interactions with the Higgs boson h are controlled by the Higgs vacuum expectation value (VEV) $v \simeq 246$ GeV and λ, a free parameter. However, very small values of λ represent a fine-tuning, because it is renormalized additively at the one loop level through diagrams such as those shown in Figure 3.1. These relate the effective value of λ at scales μ

[1]It is worth noting that Ref. [32] explored a different construction that obviates the need for a $\mathbb{Z}_2$ symmetry by having the dark matter contained in a pseudoscalar triplet that arises from a complex triplet Higgs that mixes through electroweak symmetry-breaking with the SM Higgs doublet.

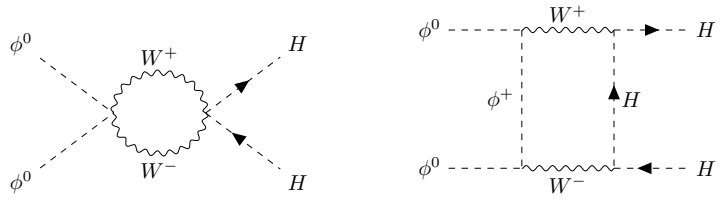

Figure 3.1: Two representative diagrams contributing to λ at one loop.

and μ_0 (keeping only log-enhanced terms):

$$\lambda(\mu) \simeq \lambda(\mu_0) + \frac{g_2^4}{\pi^2} \ln\left(\frac{\mu^2}{\mu_0^2}\right) \ , \tag{3.3}$$

which e.g. would induce $\lambda \sim \mathcal{O}(1)$ at the TeV scale if λ were taken to vanish at the GUT scale.

At tree level, the masses of the charged and neutral components are degenerate, and determined by the parameters μ_ϕ and λ,

$$m \equiv m_{\phi^0}^2 \quad = \quad m_{\phi^\pm}^2 = \mu_\phi^2 + \frac{1}{2}\lambda v^2 \ . \tag{3.4}$$

At one loop, electroweak symmetry-breaking raises the mass of the charged states, which in the limit of $m \gg v$ results in [71],

$$\Delta m \equiv m_{\phi^\pm} - m_{\phi^0} \approx 166 \text{ MeV} \ . \tag{3.5}$$

In the absence of additional ingredients, a strong degeneracy between the masses of the charged and neutral states is inevitable. If one invokes heavy physics which has been inte-

grated out, effectively giving rise to the dimension six operator,

$$\mathcal{L}_{\rm Mass} = -\frac{1}{\Lambda^2}|\phi^a H^\dagger T^a H|^2 \quad \rightarrow \quad -\frac{1}{16\Lambda^2}(\phi^0)^2(v+h)^4 \tag{3.6}$$

It will shift the mass of the neutral component by

$$\Delta m^2_{\phi^0} = -\frac{1}{16\Lambda^2}v^4, \tag{3.7}$$

allowing one to lift the degeneracy by up to ~ 200 GeV, for $\Lambda \sim$ TeV. Such an interaction would be induced, for example, by integrating out a mediator SU(2) singlet scalar field S that is odd under the dark $\mathbb{Z}_2$ and has interactions such as $S\phi^a H^\dagger T^a H$. Such a UV completion would be unlikely to further modify the phenomenology we discuss, provided the mass of the S is sufficiently larger than both the mass of ϕ^0 and the electroweak scale.

The presence of this operator also impacts couplings that can contribute significantly to the rates relevant for direct, indirect, and collider searches, shifting the interactions of ϕ^0 with one or two Higgs bosons to:

$$\left(\frac{\lambda v}{2} - \frac{v^3}{4\Lambda^2}\right)(\phi^0)^2 h \quad \text{and} \quad \frac{1}{4}\left(\lambda - \frac{3v^2}{2\Lambda^2}\right)(\phi^0)^2 h^2, \tag{3.8}$$

respectively. We will find it convenient to refer to the strength of the effective h-ϕ^0-ϕ^0 interaction as $\lambda_{\rm eff} v/2$, where:

$$\lambda_{\rm eff} \equiv \lambda - \frac{v^2}{2\Lambda^2}. \tag{3.9}$$

As discussed below, these couplings induce invisible Higgs decays and there are loose constraints on the value of Λ, which can accommodate mass splittings of up to a few hundred GeV.

3.2 Collider Constraints

The first set of constraints we consider are from the production of dark matter at high energy colliders, such as the LHC and LEP. The rich experimental programs provide multiple complimentary search methods, and probe much of the lower end of the WIMP mass spectrum. Because of the $\mathbb{Z}_2$ symmetry, the underlying production mechanisms in pp or electron-positron collisions involve producing $\phi^0\phi^0$ from Higgs exchange or W boson fusion; $\phi^+\phi^-$ via an intermediate Z, γ, or Higgs boson or from vector boson fusion; and $\phi^0\phi^\pm$ via W exchange or from $W^\pm Z$ fusion. The decay $\phi^\pm \to W^\pm\phi^0$ produces additional SM particles in the final state, which may be very soft when the mass splitting between the charged and neutral states is small. A variety of search strategies attempt to identify distinct signatures from these various DM production channels. Mono-jet searches, invisible Higgs decays, and disappearing charged tracks all apply in different regions of parameter space.

3.2.1 Invisible Higgs Decays

If kinematically allowed $m_\phi \leq M_h/2$, the coupling to the SM Higgs, Eq.(3.8), allows for Higgs decays into a $\phi^0\phi^0$ final state which escape the detectors ($h \to$ inv), leading to a striking missing energy signal. The irreducible SM background from $h \to ZZ \to 4\nu$, has a branching ratio consistent with the SM expectations $\sim 10^{-3}$ [118] leading to a bound on additional invisible Higgs decay modes, $\mathcal{B}(h \to \text{inv}) \leq 0.19$ [118]. This translates into a bound on a combination of λ and Λ via the DM contribution to the invisible Higgs decay $h \to \phi^0\phi^0$:

$$\Gamma_{h\to\phi^0\phi^0} = \frac{\sqrt{M_h^2 - 4m_{\phi^0}^2}}{16\pi M_h^2} v^2 \lambda_{\text{eff}}^2, \tag{3.10}$$

which modifies the Higgs branching ratio into an invisible final state to

$$\mathcal{B}(h \to \text{inv}) = \frac{\Gamma_{\text{DM}}}{\Gamma_{\text{SM}} + \Gamma_{\text{DM}}}. \tag{3.11}$$

Using the SM Higgs width $\Gamma_{\text{SM}} = 3.2^{+2.8}_{-2.2}$ MeV [117], λ_{eff} must be smaller than

$$\lambda_{\text{eff}} \lesssim (0.102\ \text{GeV}^{1/2}) \times \frac{1}{(M_h^2 - 4m_{\phi^0}^2)^{1/4}} \qquad (m_\phi \leq m_H/2)\,, \tag{3.12}$$

which requires $\lambda_{\text{eff}} \lesssim 10^{-2}$ for $m_{\phi^0} \ll M_h$.

3.2.2 Disappearing Tracks

Disappearing charged tracks (DCTs) provide another unique signature. This occurs when a long-lived charged particle hits multiple tracking layers, but disappears due to a decay into a neutral state and a very soft charged particle that escapes detection. In the general context of electroweak multiplet dark matter, if the degeneracy of the masses between the neutral and charged fields are only lifted by electroweak corrections, then decay products may not be able to be detected, and the charged track vanishes at the point of decay.

In the case of the electroweak triplet in the limit of only radiatively-induced mass splitting, the charged states decay $\phi^\pm \to \phi^0 \pi^\pm$. Due to the small mass splitting, the lifetime of the charged states is typically long enough for it to hit multiple tracking layers before decaying, and, the momentum of the resulting pion is too soft to be reconstructed, leading to a DCT. For decay rates governed by the electroweak interaction, the LHC is able to rule out this scenario for low ϕ masses, requiring [45]:

$$m_{\phi^0} \geq 287\ \text{GeV} \qquad (\text{Compressed Spectrum})\,. \tag{3.13}$$

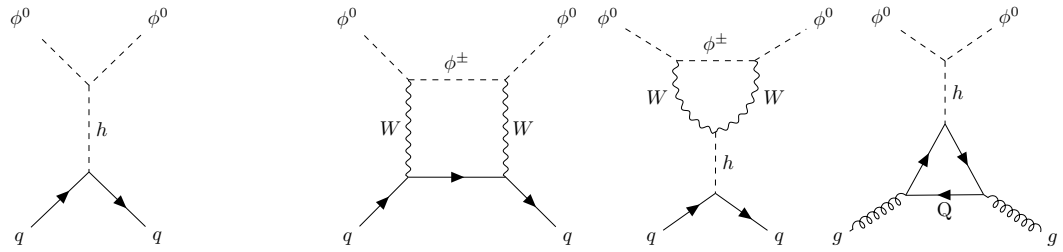

Figure 3.2: Representative Feynman diagrams for dark matter scattering with quarks/gluons at tree and one loop levels.

3.2.3 Isolated Prompt Leptons

As discussed above, heavy physics may act to induce a mass splitting between the charged and neutral ϕ states of up to about 200 GeV. The analysis of Ref. [58] argues that charged partner masses $m_{\phi^\pm} \leq 100$ GeV are ruled out for any mass splitting $\Delta m \geq 10$ GeV by a combination of searches at LEP2 combined with LHC results from mono-jet, invisible Higgs decay, and disappearing charged track searches. Generic searches by ATLAS [2, 3] and CMS [116] looking for isolated hard charged leptons are expected to have good sensitivity to production of $\phi^\pm$ followed by the decay $\phi^\pm \to W^\pm \phi^0$, but are typically interpreted in the context of specific minimal supersymmetric model parameter points, and are not always trivially recast to apply to the case at hand. Nevertheless, these searches fairly robustly exclude $m_{\phi^0} \lesssim 10$ GeV for $m_{\phi^+} \lesssim 170$ GeV [2], and a window in m_{ϕ^+} from $m_{\phi^+} \gtrsim (m_{\phi^0} + 120$ GeV) to $m_{\phi^+} \lesssim 425$ GeV for 20 GeV $\lesssim m_{\phi^0} \lesssim 100$ GeV [3]. Thus a moderately compressed spectrum for any dark matter mass above 10-20 GeV, and any uncompressed spectrum with $m_{\phi^0} \gtrsim 120$ GeV or $m_{\phi^+} \gtrsim 425$ GeV are not constrained by these searches.

3.3 Direct Searches

An important class of constraints on any WIMP come from the null results of searches for the ambient dark matter populating the neighborhood of the Solar System scattering

with terrestrial targets. The strongest constraints on WIMPs are typically from experiments searching to detect scattering with heavy nuclei. Given the low expected velocity of Galactic dark matter, the typical momentum transfer is expected to be less than the typical nuclear excitation energies, and the elastic scattering can be described by an effective field theory containing nuclei as degrees of freedom. The nuclear physics is typically unfolded as part of the experimental analysis, and the exclusion limits presented as limits on the spin-independent (SI) or spin-dependent (SD) cross section for scattering with protons or neutrons, extrapolated to zero momentum-transfer [87].

At tree-level, the coupling to the SM occurs through Higgs exchange via $\lambda_{\rm eff}$, whereas at loop level there are also electroweak contributions [71] (see Figure 3.2). Integrating out the Higgs and heavy quarks leads to a spin-independent scalar coupling to quarks and gluons,

$$\mathcal{L}_{\rm SI} = \frac{\lambda_{\rm eff}\ m_q}{2M_h^2}(\phi^0)^2\bar{q}q - \frac{\lambda_{\rm eff}\ \alpha_s}{24\pi M_h^2 v}(\phi^0)^2 G^{\mu\nu}G_{\mu\nu}\ , \tag{3.14}$$

which are mapped onto an effective coupling to nucleons via the matrix elements [87]:

$$\langle n(k')|m_q\bar{q}q|n(k)\rangle \equiv m_n f^n_{T,q}\bar{u}(k')u(k) \tag{3.15}$$

$$\langle n(k')|\alpha_s G^{\mu\nu}G_{\mu\nu}|n(k)\rangle \equiv -\frac{8\pi}{9}m_n f^n_{T,g}\bar{u}(k')u(k)\ , \tag{3.16}$$

parameterized by the quantities $f^n_{T,q}$ and $f^n_{T,g}$. The spin independent cross section is

$$\sigma_{\rm SI}(\phi\ n \to \phi\ n) = \frac{\lambda^2_{\rm eff}}{4\pi m_\phi^2}\frac{\mu^2_{\phi n}m_n^2}{M_h^4}\left(f^n_{T,u} + f^n_{T,d} + f^n_{T,s} + \frac{2}{9}f^n_{T,g}\right)^2 \tag{3.17}$$

where m_n is the mass of the nucleon, and $\mu_{\phi n}$ is the reduced mass and the f^n_T approximately satisfy $f^n_{T,u} + f^n_{T,d} + f^n_{T,s} + \frac{2}{9}f^n_{T,g} \approx 0.29$ [15, 14, 59]. Because the Higgs coupling is dominated by heavy quarks (contributing through loops to the gluon operator), the scattering with nucleons is approximately isospin symmetric.

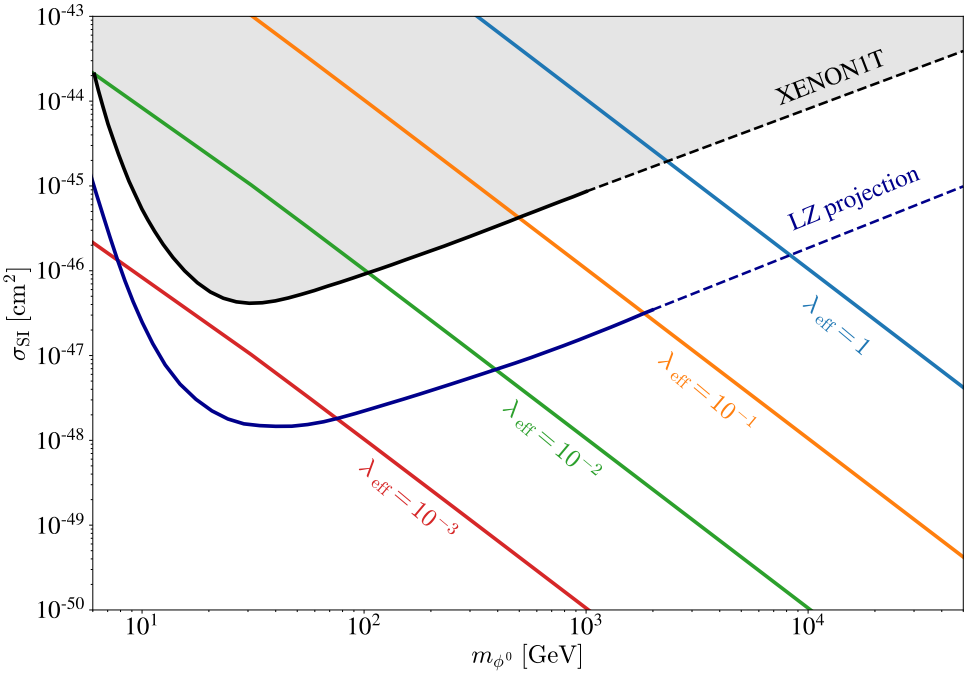

Figure 3.3: Spin-independent cross section for various values of $\lambda_{\rm eff}$, as indicated. The current bounds from XENON1T (black) and the projected future sensitivity from LZ (violet) are also indicated.

Neglecting the small electroweak loop contributions (which, due to partial cancellations, would result in a very small scattering rate of order $10^{-(47-48)}$ cm^2 [72] – far below the reach of current direct searches), we show the spin independent cross section as a function of the dark matter mass for several choices of $\lambda_{\rm eff}$ in Figure 3.3. Also shown are the current limits on $\sigma_{\rm SI}$ from the null results of the search for dark matter scattering by XENON1T [18], and projected limits from the LZ experiment [12]. Evident from the figure, XENON1T places an important upper limit on the allowed values of $\lambda_{\rm eff}$ for a given dark matter mass. To be consistent with any choice of dark matter mass requires,

$$\lambda_{\rm eff} \lesssim 10^{-3}, \tag{3.18}$$

with larger values of $\lambda_{\rm eff}$ permitted for dark matter masses $\gtrsim 30$ GeV or $\lesssim 10$ GeV. Moving

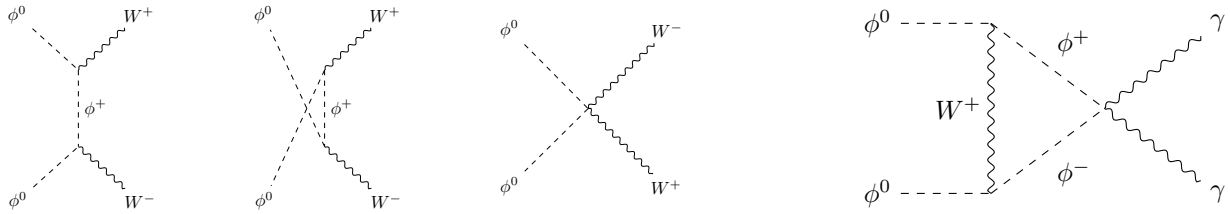

Figure 3.4: Representative Feynman diagrams for dark matter annihilation into W^+W^- at tree level (left), or into two mono-energetic photons at loop level (right).

forward, we adopt $\lambda_{\text{eff}} \simeq 10^{-3}$ as a benchmark when we discuss indirect searches, below.

3.4 Indirect Searches

Searches for dark matter annihilation in the present day universe provide a complimentary probe of dark matter parameter space, with typical targets including the galactic center (GC) and dwarf spheroidal galaxies (dSphs). We focus on the case of production of high energy gamma rays in dark matter annihilation, which are experimentally accessible over a wide range of energies, and for which the direction of their origin can be measured, providing an additional handle to analyze the dark matter signal. The GC leads to a large potential signal from annihilation, but observations suffer from large astrophysical uncertainties and necessarily complicated regions of interest (RoIs). On the other hand, dSphs provide a lower density source, but generally have much lower backgrounds and uncertainties. Additionally, since there are a variety of dSph Milky Way satellites, stacked analyses can combine the observations to yield stronger and more robust constraints [8].

We consider two important dark matter annihilation processes producing energetic photons: tree level production of continuum photons, and loop level production of mono-energetic gamma ray lines (see Figure 3.4). At tree level, neglecting the effects of λ_{eff} which we assume for now to be negligibly small, the dark matter can annihilate into a W^+W^- final state that can directly radiate photons; produce them through decays into neutral pions; or

produce electrons that radiate via interactions with the interstellar medium and magnetic fields. The predicted gamma ray flux generically depends on the annihilation rate and the distribution of the dark matter within the RoI:

$$\frac{d\Phi}{dE_\gamma}(E_\gamma, \psi) = \frac{\langle \sigma v \rangle}{8\pi m_{\phi^0}^2} \sum_i B_i \frac{dN_i}{dE_\gamma} \times J(\psi) \tag{3.19}$$

where $\langle \sigma v \rangle$ is the total annihilation cross section; B_i and dN_i/dE_γ are the branching fraction and the photon spectrum for final state, i, which fully characterize the particle physics information; and

$$J(\psi) \equiv \int d\Omega \int_{\text{los}} \rho^2 ds \tag{3.20}$$

is the J-factor for dark matter annihilation, encoding the information about the density of the dark matter along the line of sight of the observation centered on an angle ψ with respect to the axis from the Earth to the center of the Galaxy.

3.4.1 Annihilation Cross Sections

For dark matter masses above the W mass, the annihilation is dominated by annihilation into on-shell W^+W^-, whereas for $M_W/2 \lesssim m_{\phi^0} \leq M_W$ the dominant configuration has one W on-shell, and the other off-shell, and for $m_{\phi^0} \leq M_W/2$, both W's are forced to be off-shell. For $m_{\phi^0} \geq M_W$, the cross section in the zero relative velocity limit reads:

$$\langle \sigma_{WW} v \rangle = \frac{\sqrt{m_{\phi^0}^2 - M_W^2}}{8\pi m_{\phi^0}^3} \left(g_W^4 \left(\frac{M_W^4}{(M_W^2 - 2m_{\phi^0}^2)^2} + 2 \right) + \frac{6 g_W^2 \lambda_{\text{eff}} M_W^2}{M_h^2 - 4m_{\phi^0}^2} + \frac{\lambda_{\text{eff}}^2 (3M_W^4 - 4M_W^2 m_{\phi^0}^2 + 4m_{\phi^0}^4)}{(M_h^2 - 4m_{\phi^0}^2)^2} \right) \tag{3.21}$$

where the second and third terms may typically be neglected for our benchmark value of $\lambda_{\text{eff}} \sim 10^{-3}$. For dark matter masses below M_W, we compute the annihilation into the open

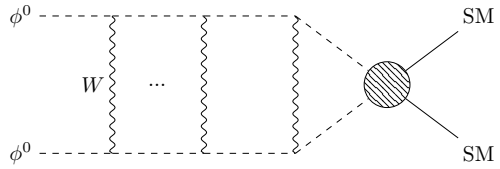

Figure 3.5: Ladder diagram illustrating the non-perturbative effect of a long-range potential leading to a Sommerfeld-like enhancement.

final states numerically using the MadDM package [16].

The search for mono-energetic gamma ray lines through $\phi^0\phi^0 \to \gamma\gamma$ and $\phi^0\phi^0 \to \gamma Z$ is of particular importance for large dark matter masses in some theories, where the striking signature can balance a suppressed loop-level amplitude [78]. In the limit of large dark matter mass, $m_{\phi^0} \gg M_W$ and $m_{\phi^0} \gg \Delta m$, the cross section for annihilation into $\gamma\gamma$ simplifies considerably, and was computed in Ref. [47] to be

$$\langle \sigma_{\gamma\gamma} v \rangle = \frac{4\pi\alpha_{EM}^2\alpha_W^2}{M_W^2}\left(1+\sqrt{\frac{2\Delta m m_\phi}{M_W^2}}\right)^{-2}, \tag{3.22}$$

where the last factor provides an important correction at large m_ϕ [60]. The rate for annihilation into γZ in the same limit is related by $\mathrm{SU}(2)_{\mathrm{EW}}$ gauge invariance [109]:

$$\langle \sigma_{\gamma Z} v \rangle = \frac{6\pi\alpha_{EM}\alpha_W^3}{M_Z^2}\left(1+\sqrt{\frac{2\Delta m m_\phi}{M_W^2}}\right)^{-2}. \tag{3.23}$$

These expressions provide a good qualitative guide to the behavior of the cross sections, but for our quantitative analysis we adopt the calculations of $\phi^0\phi^0 \to \gamma\gamma$ and $\phi^0\phi^0 \to \gamma Z$ from Ref. [110], which also contain relevant sub-leading contributions and important re-summation of higher order effects.

3.4.2 Sommerfeld Enhancement

At low velocities, there are potentially important corrections to the annihilation cross section from Sommerfeld-like enhancements originating from formally higher order ladder diagrams such as the one illustrated in Figure 3.5 [73]. These diagrams encode the additional effective cross section for annihilation due to a long-range attraction between the incoming dark matter particles. The enhanced cross section can be parameterized as

$$\sigma v = S \times \langle \sigma_0 v \rangle \tag{3.24}$$

where $\langle \sigma_0 v \rangle$ is the leading order annihilation cross section, and S represents the impact of the Sommerfeld enhancement, given schematically for the case of a strictly massless mediator by

$$S \sim 1 + \frac{\alpha_W}{v} + ... \ . \tag{3.25}$$

At the low velocities characteristic of the dark matter in the Galaxy ($\sim 10^{-3}$) or in dSphs ($\sim 10^{-5}$), the enhancement for a massless mediator would be a large effect. However, the finite (electroweak size) mediator mass results in a Yukawa potential, for which the Sommerfeld enhancement generically scales more like [23]:

$$S \sim 1 + \alpha_W \frac{m_\phi}{M_W} \ . \tag{3.26}$$

No closed form expression exists for the Sommerfeld enhancement arising from a Yukawa potential, and we evaluate it numerically. S is strongly depending on both the relative masses of the dark matter and mediator, and the typical velocity of the dark matter. As a result, $\langle \sigma v \rangle$ can differ for e.g. the Galactic center and the dwarf spheroidal galaxies. Where necessary, we provide annihilation cross sections for both, to be compared with the

corresponding relevant bound.

3.4.3 J Factor

The J-factor depends on the dark matter profile of the source, $\rho(\vec{r})$, which is often not well known. There is wide discussion in the literature concerning which profiles are suggested by data and/or simulations of galaxy formation. Current data is consistent with both cuspy and cored profiles [79, 100]. Pure DM galactic simulations tend to favor cuspy profiles. However, including baryons in simulations provides feedback processes that can smooth the cusps into cores as large as order $\sim$ kpc [44, 95]. An examples of a cuspy and distribution often used in the literature is the Einasto [64] profile given by

$$\rho_{\rm Ein}(r) = \rho_s \exp\left\{ -\frac{2}{\alpha}\left(\left(\frac{r}{r_s}\right)^{\alpha} - 1\right)\right\}, \tag{3.27}$$

where α and r_s are parameters typically extracted from simulations [107]. While Einasto is fully consistent with observation, the data also permit profiles with large cores, such as e.g. the Burkert [42] profile, as well.

For small RoIs in the direction of the Galactic Center, the uncertainties in the profile result in a dramatic range of possible J factors, which translate into a wide spread of possible bounds on the annihilation cross section. The H.E.S.S. GC observations place strong constraints on WIMP annihilation when the cuspy Einasto profile is chosen, whereas a cored profile leads to much weaker bounds [4, 60, 50]. This is due in part to the strategy that H.E.S.S. uses to determine its background rate, by comparing a slightly off-center control region (OFF) to the signal (ON) region centered on the Galactic center. As the control region is within about $\sim$ 450 pc of the GC, a $\sim$ kpc sized core would require an accurate extrapolation of the background from the OFF to the ON region to provide a meaningful limit [110]. We simulate cored profiles by assuming an Einasto profile outside of the core radius, with

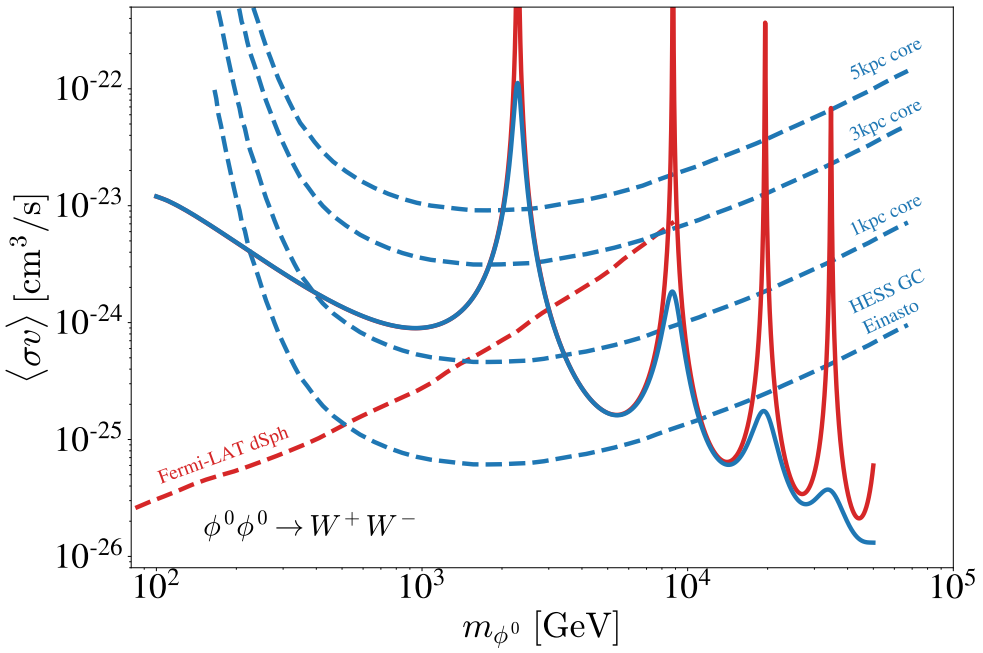

Figure 3.6: The annihilation cross section for $\phi^0\phi^0 \to W^+W^-$ including the Sommerfeld enhancement with velocities consistent with the galactic center (light blue), and dwarf spheroidal galaxies (orange) for comparison with H.E.S.S. (dark blue) and Fermi-LAT (red) bounds on this annihilation channel based on gamma rays, respectively.

a constant density inside the core. Fortunately, the profiles of dwarf spheroidal galaxies, which are anchored by measurements of stellar kinematics, are much less uncertain than the Galactic center, and thus generally provide more robust constraints [105] (but see also [17]).

3.4.4 Bounds from Indirect Searches

In Fig. 3.6, we show the predicted annihilation cross section for $\phi^0\phi^0 \to W^+W^-$, including the Sommerfeld enhancements expected for the typical dark matter velocity in the Milky Way (MW) Galaxy and in a dwarf spheroidal galaxy. Also shown for comparison are the bounds derived from measurements of gamma rays, interpreted for the W^+W^- final state channel, from the Fermi-LAT observations of dSphs [8] and the H.E.S.S. observations of the GC [6]. For the H.E.S.S. observations, we represent the impact of the uncertainty in the dark

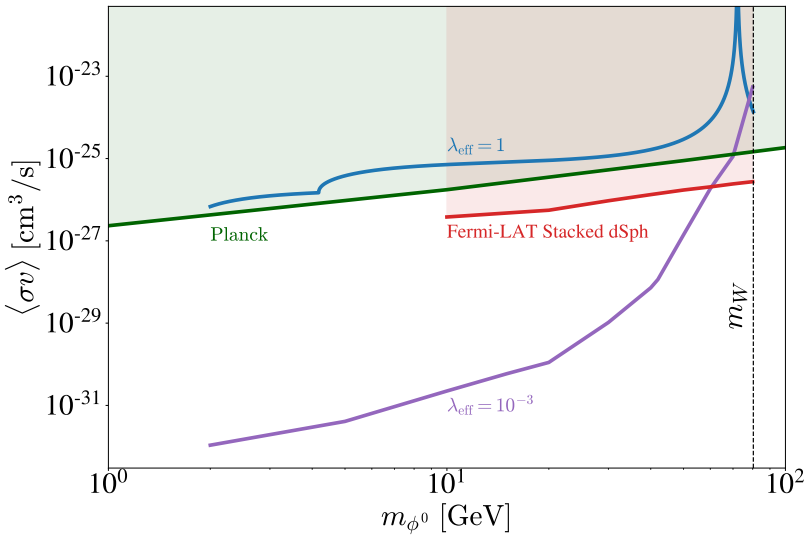

Figure 3.7: Annihilation cross sections for inclusive gamma ray and positron production when the ϕ^0 mass is below M_W for $\lambda_{\rm eff} = 1$ (blue) and $\lambda_{\rm eff} = 10^{-3}$ (purple), and the corresponding limits on that quantity from Fermi-LAT observations of dwarf spheroidal galaxies (red), derived from the likelihood analysis of MadDM [16], as well as the CMB limit (green) derived using the spectra of e^+ and e^- generated by MadDM.

matter profile by showing limits for an Einasto profile, as well as for cored profiles with 1 kpc, 3 kpc, and 5 kpc cores. The resulting bounds vary over roughly two orders of magnitude, and for more extremely cored profiles, H.E.S.S. fails to rule out any of the parameter space that is not already excluded by Fermi-LAT[2]. Limits by Fermi from observations of dwarf spheroidals exclude masses from M_W to about ~ 3 TeV. For larger masses, H.E.S.S. extends the region ruled out up to ~ 10 TeV if the profile at the Galactic center is described by Einasto, but little beyond Fermi if the Galactic profile has a core.

As discussed above, for $m_\phi < m_W$, one or both of the W's is forced to go off-shell, leading to more complicated final states including $\phi\phi \to W^\pm ff$ and $\phi\phi \to ffff$. The experimental collaborations limit their presentation of deconvolved bounds to two-body final states, meaning that no careful analysis of the gamma ray spectrum for these final states is read-

[2]It is also worth noting that using the full γ-ray spectrum from WIMP annihilation, H.E.S.S. excludes a small region around $m_\phi \sim 2.3$ TeV with a stacked analysis of dSph observations [5].

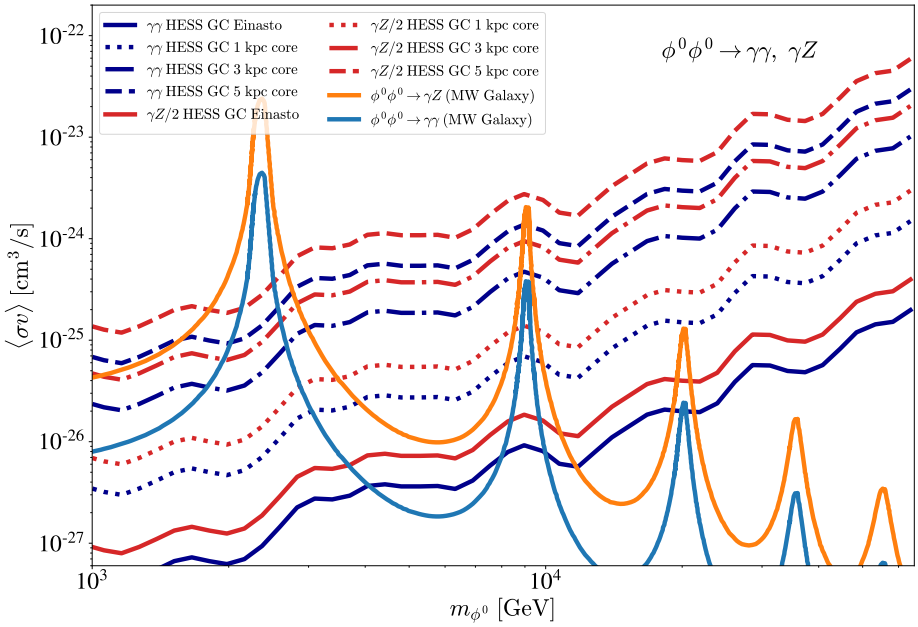

Figure 3.8: The annihilation cross section for $\phi^0\phi^0 \to \gamma\gamma$ (light blue) and $\phi^0\phi^0 \to \gamma Z$ (orange) based on the re-summed calculation of Ref. [110] for comparison with H.E.S.S. bounds from searches for gamma ray lines for different dark matter profiles (dark blue and red families of curves, respectively.

ily available from them. To understand the limits below M_W, we numerically compute the spectrum of gamma rays for these states using MadDM [16] and use its built-in likelihood analysis to compare with the raw bound on dark matter contributions from the Fermi-LAT observation of the dSphs. The predicted cross section for the inclusive gamma ray spectrum, and the bound derived from it, are shown in Figure 3.7. In this regime of masses, Fermi-LAT excludes masses in the range 10 GeV $\geq m_\phi \geq$ 60 GeV.

The rates for annihilation into $\gamma\gamma$ and γZ are shown (for Galactic velocities) in Figure 3.8, along with the corresponding limits on mono-energetic gamma ray features from H.E.S.S. observations of the inner Galaxy [7] for the Einasto and three differently sized cored profiles. The $\gamma\gamma$ and γZ searches exclude a similar parameter space to the ones derived from annihilation into WW or an Einasto profile, with an additional region probed at the third

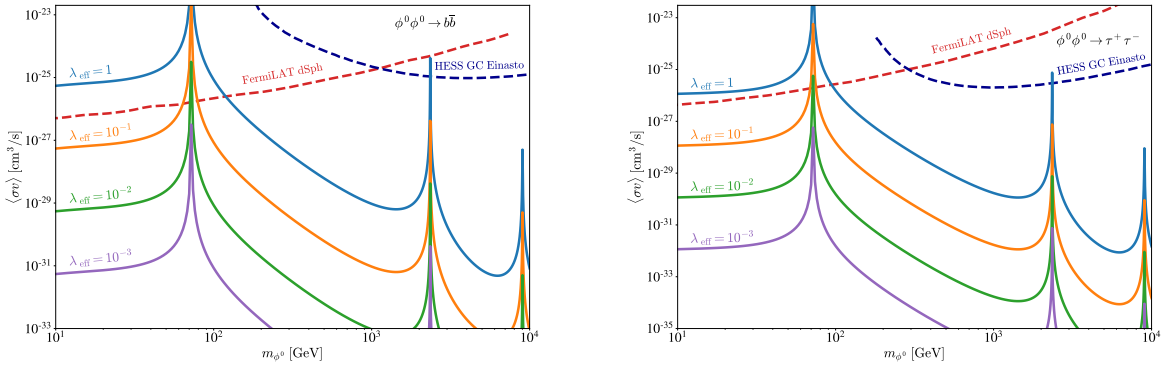

Figure 3.9: Annihilation cross sections for $\phi^0\phi^0 \to b\bar{b}$ (right panel) and $\phi^0\phi^0 \to \tau^+\tau^-$ (left channel) for different values of $\lambda_{\rm eff}$ as indicated. Also shown are limits on these channels from gamma ray observations by Fermi-LAT (black) and H.E.S.S. (purple).

Sommerfeld resonant peak at ~ 20 TeV.

Finally, so far in discussing the bounds from indirect searches we have assumed that $\lambda_{\rm eff}$ is $\leq 10^{-3}$ to avoid the strong constraints on it from direct searches discussed in Section 3.3. In order to compete effectively with the annihilation into W pairs, either the mass of the dark matter should be far below M_W, or $\lambda_{\rm eff}$ should be $\gtrsim g_2$, which is consistent with the bounds from XENON1T provided $m_\phi \gtrsim 1.5$ TeV. There is also a tiny region that is resonantly enhanced around $m_\phi \simeq M_h/2$. The Higgs coupling can mediate annihilation to hh for $m_\phi \geq M_h$, or to $\bar{f}f$, dominated by the heaviest fermion kinematically accessible below that. In Figure 3.9, we show the expected cross sections for annihilations into the two most important channels, $b\bar{b}$ and $\tau^+\tau^-$, for various values of $\lambda_{\rm eff}$. Comparing with the existing bounds from Fermi and H.E.S.S., it is clear that they do not currently provide additional information beyond the combined requirements of direct searches and limits on annihilation into on-shell or off-shell W bosons.

3.4.5 Constraints from CMB Observables

Precision measurements of the Cosmic Microwave Background (CMB) offer an important vista on dark matter annihilation at late times. A wealth of literature has established the tools to constrain dark matter models using the CMB (see e.g. [119, 120, 89, 88]), which can be particularly stringent for light masses. The *Planck* Collaboration provides a robust bound on the annihilation parameter of $f_{\rm eff}\langle\sigma v\rangle/m_\phi < 4.1\times10^{-28}{\rm cm}^3/{\rm s/GeV}$ [10], where $f_{\rm eff}$ is the spectrum-weighted efficiency factor [119]. We generate the spectra of e^+ and e^- from $\phi\phi$ annihilation into all kinematically accessible two, three, and four-body final states for dark matter masses in the GeV to TeV range using MadDM [16], from which (following Ref. [119]) we extract the spectrum-weighted $f_{\rm eff}$. The *Planck* bound thus translates into a bound on the annihilation cross section which is compared to the predicted annihilation cross section in Figure 3.7. At very low masses, the two-body final states through the Higgs portal dominate the spectrum for all values of the Higgs portal coupling down to $\lambda_{\rm eff} \simeq 10^{-3}$, and produce CMB bounds that are roughly independent of the values of $\lambda_{\rm eff}$ we consider. For $\lambda_{\rm eff} \simeq 1$, the CMB independently excludes masses up to ~ 700 GeV. For $\lambda_{\rm eff} = 10^{-3}$, the CMB excludes $70\ {\rm GeV} \lesssim m_\phi \lesssim 500\ {\rm GeV}$. In both of these cases, the CMB constraints exclude regions of the parameter space that are also excluded by the other complementary search methods. Nonetheless, since they involve different systematics and are not sensitive to the detailed J-factors of astrophysical targets, they provide essential complementary information.

3.5 Conclusions

The question as to the viability of WIMP dark matter remains a subtle one, which in some sense reflects choices as to how to define terms as much as physics. We examine the constraints on real massive scalar particles with full strength electroweak interactions (as triplets) whose abundance in the early Universe is not explicitly tied to standard freeze-

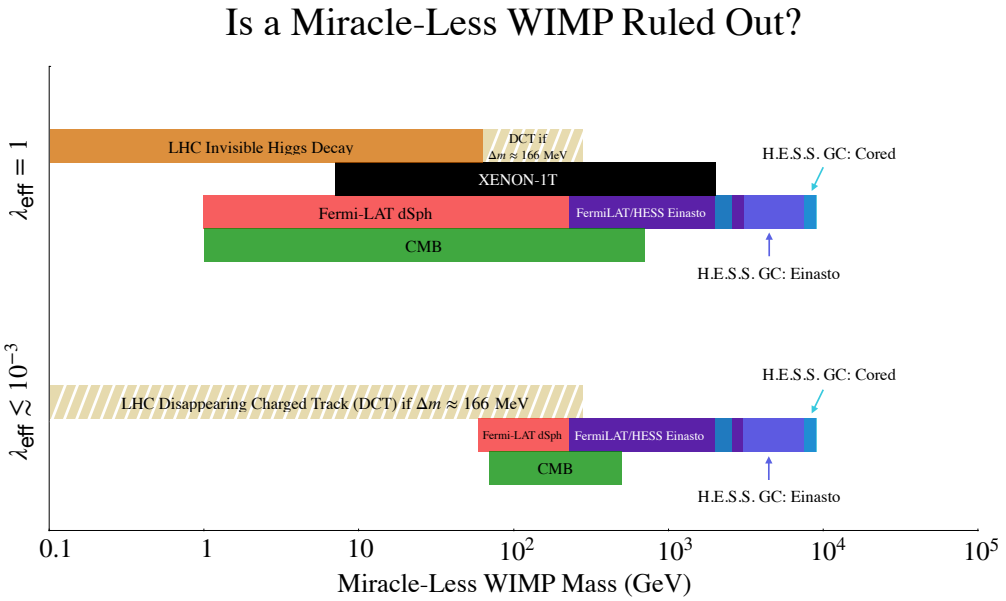

Figure 3.10: Summary of the constraints on an electroweak triplet real scalar field as dark matter.

out (a situation which may be referred to as a 'miracle-less WIMP'). Such particles very naturally have properties placing them in the right ballpark to play the role of dark matter, without the prejudice on their parameter space implied by the assumption that they froze out during the evolution of a standard cosmology. Their properties are generally captured by three quantities: the mass of the dark matter, the mass of its charged SU(2) sibling, and a dimensionless coupling to the Standard Model Higgs. The strength and form of the inevitable coupling to the electroweak bosons dictated by gauge invariance is already fixed by the measured SM couplings e and $\sin\theta_W$.

It has been known for some time that the value of the mass for which the WIMP miracle occurs, $m \sim 2$ TeV, is reliably excluded by indirect searches. A summary of the exclusions from various search strategies is presented in Figure 3.10. Direct searches, often the most stringent constraints on WIMPs, rule out a large range of masses for large values of the Higgs coupling, but are currently unable to say much if this coupling is less than about 10^{-3}. A Higgs interaction this small is similarly difficult to discern in rare Higgs decays at the LHC (provided the dark matter is light enough for the Higgs to decay into it) and more

direct LHC searches are operative only at very low masses, or for specific large (or tiny) mass splittings between the charged and neutral states. They fairly robustly exclude this scenario for dark matter masses below about 10 GeV, but otherwise can typically be evaded for a moderately compressed spectrum. It is conceivable that a more directed LHC analysis strategy could close the window on a larger swath of the parameter space.

Indirect searches are subject to large uncertainties in the J factor due to our imperfect knowledge of how dark matter is distributed in astrophysical targets, but do provide key information that does not rely on a large Higgs portal coupling strength. Even for small $\lambda_{\rm eff}$, a range of masses from around 60 GeV to a few TeV can be reliably excluded by Fermi if the dark matter profile of the Galaxy turns out to have a large core. For a cuspy profile such as Einasto, H.E.S.S. excludes additional parameter space up to around 10 TeV.

Much viable parameter space for a miracle-less scalar electroweak triplet as dark matter remains, albeit constrained in interesting ways which highlight the complementarity of the various search strategies [37]. Our study exemplifies the need for better experimental coverage of the parameter space in order to properly answer the question as to whether simple WIMP models are excluded, or perhaps are present as dark matter but taking an inconvenient incarnation for our current searches.

Chapter 4

Annihilogenesis

This chapter heavily relies on previously published work in collaboration with Arvind Rajaraman and Tim M.P Tait [20]

In this chapter, we investigate a FOPT producing a large shift in the mass of a BSM particle χ, and explore how this leads to an interesting interplay between the role of χ decay and $\chi\chi$ annihilation into SM particles during the FOPT itself. After bubbles of the true vacuum nucleate, the χ mass can be radically different inside and outside. As the bubbles expand and collide (using the terminology of Ref. [24]), segmented "pockets" of unbroken phase remain, and experience contraction as the bubbles grow to fill the entire Universe. While this happens, χ particles in the pockets reflect off the bubble walls due to the large $M_\chi^{\rm in}/T$ in the broken phase and as a result are trapped in the pockets,"squeezing" them together.

We focus on the interplay between decay and annihilation processes during the pocket collapse, and analyze under which situations one or the other can become the dominant mechanism depleting the particles. Generically, one would expect that decays, if allowed, would dominate over annihilation processes such that the depletion is governed by the decays alone.

However, as they are squeezed inside a contracting pocket, the particle densities may grow large enough to provide enough enhancement of the annihilation rate that a significant number of χ annihilate rather than decay, even for large decay widths. We find that depending on the parameters of the theory, the decay and annihilation can compete or be relevant at different times during the phase transition. This mechanism thus provides a novel relationship between the depletion processes, and can open up large regions of the parameter space in which annihilation can become important or even dominate over decay.

As a specific application, we apply this scenario to baryogenesis. Interference between tree-level and loop-level diagrams can lead to a CP asymmetry in both decay and annihilation, and even if the decay and annihilation processes are governed by the same couplings (which they need not be), there are additional contributions to a CP asymmetry from the annihilation processes, and therefore the asymmetries generated by decay and annihilation are not constrained to be the same. We work in a generic framework, in which a FOPT traps the particles to decay or annihilate in the pockets of unbroken phase. Previous related work [31, 26] has examined baryogenesis in a similar context with relativistic bubble walls, but under the assumption that the effect of reflection off of the bubble walls is negligible.

Recent studies have investigated similar ideas in the context of dark matter (DM), and how the DM relic abundance may be set by interactions with non-relativistic bubble walls via a "filtering" effect [76, 68, 30, 46], leading to an exponentially suppressed abundance of DM inside the bubbles. The DM relic abundance has been studied in the context of ultra-relativistic bubble wall as well [27]. Other work has focused on the fate of the DM particles that reflect off the bubble wall and are trapped in the unbroken phase. The particles trapped in the pockets are eventually "squeezed" together, leading to a number of possible outcomes, depending on the specifics of their interactions. The squeezing could enhance their annihilation rate, which may determine the DM relic density [24], or increase the density sufficiently enough to create compact objects such as primordial black holes or Fermi-balls

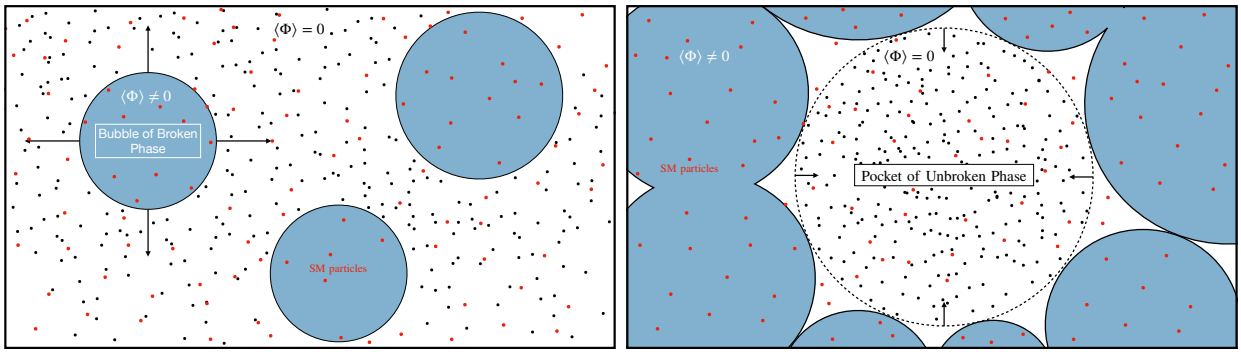

Figure 4.1: A cartoon depiction of the bubbles nucleating and expanding (left). As these bubbles collide, they create contracting pockets of unbroken phase, which trap and squeeze χ particles (black), enhancing their density (right), whereas SM particles (red) are able to traverse unimpeded. We approximate the contracting pockets to be spherical.

[74, 66, 29, 90, 80], which may themselves play the role of dark matter in the Universe today.

This chapter is organized as follows. Section 4.1 introduces the general framework and outlines the relevant features of a first order phase transition. Section 4.2 examines the interplay between decay and squeezed annihilation via the Boltzmann equation, and determines whether decay or annihilation is the dominant depletion process. Section 4.3 discusses the asymmetry that is generated for different amounts of decay and annihilation. Section 4.4 shows the gravitational wave spectrum that could be produced within this general framework. We reserve section 4.5 for our conclusions and outlook.

4.1 General Scenario

We consider a scenario where a fermion χ is coupled to a complex scalar Φ described by the Lagrangian,

$$\mathcal{L} = \overline{\chi}(i\not{D})\chi - y\Phi\overline{\chi}\chi + \text{h.c.} - \text{V}(\Phi) \tag{4.1}$$

where we assume for simplicity that both χ and Φ are SM singlets. In order to consider a wide spectrum of scenarios, we assume that there are couplings which mediate both the decay and annihilation of χ into appropriate SM states, but do not specify their specific form.

To successfully realize baryogenesis, there must be a source of CP violation in either the new sector itself or couplings between the new sector and the SM. If there are multiple flavors of χ_i, this CP violation may come directly from the Φ couplings,

$$\mathcal{L}_{CP} \supset y_{ij}\Phi\overline{\chi}_i\chi_j + y^*_{ij}\Phi^*\overline{\chi}_j\chi_i \tag{4.2}$$

which could generate CP violation via vertex corrections, self-energy corrections, and other loop level processes involving Φ. For now, we consider χ to be the lightest species of the multiple generations, with any heavier states showing up only inside these loop-level processes. The Sakharov conditions additionally require the presence of C and baryon number violation, which constrains the space of the generic couplings.

We assume that the thermal potential for Φ is such that at some temperature in the early Universe it undergoes a first order phase transition, nucleating bubbles in the process. The form of Eq. (4.1) is such that at temperatures above the Φ phase transition, the χ have zero tree level mass. After the Φ phase transition, the χ are massive inside the bubbles of broken phase (the phase where Φ has a vev) and their mass is $M_\chi^{\text{in}} = y\langle\Phi\rangle$. If the ratio $M_\chi^{\text{in}}/T \gg 1$, then only the high momentum modes of χ can penetrate the bubble wall, resulting in a large number of the χ particles being trapped in the unbroken phase. Altogether this amounts to an out-of-equilibrium process with C, CP, and baryon number violation: all of the necessary ingredients to generate a baryon asymmetry.

Throughout the remainder of the chapter, we will use terminology introduced in Ref. [24]. The regions we refer to as bubbles are the usual FOPT bubbles that nucleate and expand.

As these bubbles collide, segmented regions of unbroken phase contract, which we refer to as "pockets".

As the bubbles nucleate and expand, the particles with insufficient kinetic energy to enter the broken phase reflect off the bubble wall. The bubbles eventually collide, and isolated pockets of unbroken phase are left to contract (see Fig. 4.1). During this pocket collapse, both decay and annihilation processes can both be important in the depletion of χ as shown in Fig. 4.2 for a specific choice of parameters. Although the tree-level mass is zero in the unbroken phase, the thermal mass can allow the decays to become kinematically accessible. If the decay lifetime of χ is shorter than the collapse time, then the χ will start depleting via decays. Simultaneously, the pocket contracts, enhancing the annihilation processes as the pocket squeezing increases the density of the leftover χ. Whether the decay or annihilation processes dominate in depleting the χ abundance depends on the relationship between the decay width, Γ_χ, annihilation cross section, $\langle\sigma v\rangle$, and the pocket collapse rate.

4.1.1 Phase Transition

In general, the properties of the phase transition are largely governed by the potential $V(\phi)$ (including thermal corrections). Typically (even in the absence at tree-level), a cubic term arises from the high temperature expansion of the thermal loop corrections. This creates a barrier between the two minima, inducing a first order phase transition. By expanding the scalar field as $\Phi = (v + \phi)/\sqrt{2}$, one can generically write the finite temperature potential as [81]

$$V(\phi, T) = D(T^2 - T_0^2)\phi^2 - ET\phi^3 + \frac{\lambda(T)}{4}\phi^4 \tag{4.3}$$

with $D,\ E,$ and λ(T) determined by a combination of tree level potential parameters and both thermal and zero-temperature loop corrections. These parameters determine the critical

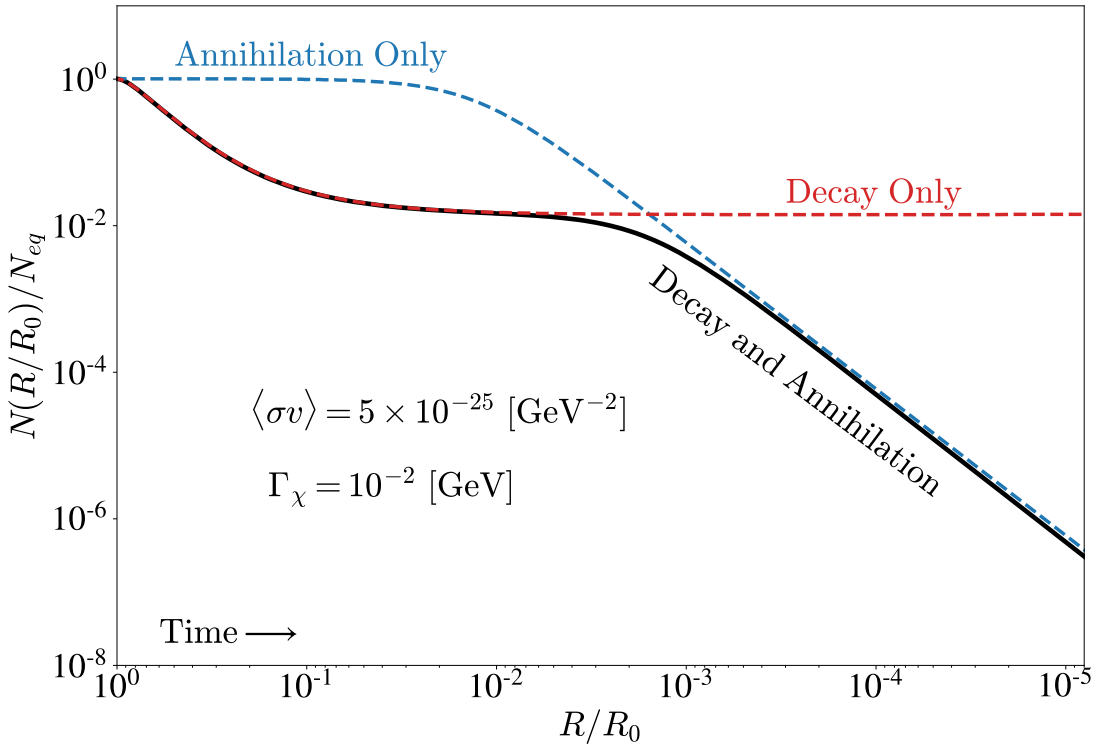

Figure 4.2: Example of χ evolution during the pocket collapse, showing the fraction of the χ that are present at different radii as the pocket collapses in cases where only decay processes are present (red), only annihilation processes are present (blue), and both decay and annihilation processes are present (black).

temperature, T_c, nucleation temperature, T_n, and the strength of the phase transition, with a strong first-order phase transition satisfying the condition $\langle\Phi\rangle/T_c \sim E/\lambda(T_c) \gg 1$. In a specific theory, the coefficients D, E, and λ can be computed, where E typically is generated by bosonic fields coupled to ϕ. For example, if the vev of ϕ is responsible for breaking a new gauge symmetry, loops including the gauge bosons in the theory would be responsible for generating the finite temperature cubic term in the potential, and E would be calculable from those loops. A strong FOPT could then be satisfied via substantial gauge couplings, generating a large E, as well as modest quartic couplings. Rather than get distracted by these specific details however, we treat them as parameters that we can freely tune to realize a FOPT with various properties. We also assume that the phase transition completes quickly

enough that the temperature can be treated as a constant throughout its progress.

The typical initial size of the pockets will directly influence the dynamics and timescales that govern the χ particles during the pocket collapse. The average number of bubbles that nucleate per Hubble volume scales as $N_b \sim \beta_H^3$, where β_H, is typically of order $\mathcal{O}(10 - 10^4)$ for strongly FOPTs [31], but could be as large as $\mathcal{O}(10^{11})$[91]. This determines the initial size of the pockets by specifying the number density of bubbles that nucleate, $n_b \sim \beta_H^3 H^3$, and the distance between bubble centers scales as $d_b \sim n_b^{-1/3} \sim R_H/\beta_H$ where $R_H \equiv 1/H$ [93]. We consider both small and large initial pocket sizes by exploring two representative choices of the initial radii, $R_0 = R_H$, and $R_0 = 5 \times 10^{-6}\, R_H$.

The bubble wall velocity v_w influences the rate at which the pockets contract. v_w can be estimated as $\sim (T_c - T)/T_c$ [129], which however this neglects the pressure exerted by χ particles reflecting off the wall, which could slow down the bubble expansion considerably [24, 29, 90]. We consider both relativistic and non-relativistic wall velocities, where the larger the wall velocity, the larger the mass needs to be in the broken phase in order to trap χ in the pockets. We choose $v_w = 0.9$, $M_\chi^{\rm in}/T = 10^2$ and $v_w = 10^{-3}$, $M_\chi^{\rm in}/T = 10$ as two representative examples, and assume that the wall velocity is approximately constant throughout the phase transition.

4.2 Decays and Squeezed Annihilation

Throughout the process of collapse, interactions with the thermal bath generate a thermal mass for χ of order $\Pi_\chi^2 \sim g^2 T^2$ (where g represents a generic coupling to the thermal bath). The particles that are trapped in these pockets are subsequently squeezed together and effectively obtain a Casimir mass, $M_\chi^{\rm cas} \sim 1/R$, where R is the pocket radius. This Casimir energy is an inherently quantum mechanical effect, due to the χ wave-functions' energies

being bounded from below because of the size of the pocket they are confined within. For sufficiently confined χ, this mass can allow χ to rapidly decay even when its tree level/thermal mass would otherwise forbid it from doing so. We denote the decay width of χ in the pocket as Γ_χ. We further assume that $\chi\chi$ is also able to annihilate into SM final states with an annihilation cross section $\langle\sigma v\rangle$.

As the pocket radius decreases to $R \sim 1/M_\chi^{\rm in}$, the Casimir energy overcomes the potential energy barrier between the unbroken and broken phases, and the remaining abundance of χ is forced into the bubbles where they eventually decay away. In Fig. 4.2, we show an example of the evolution of the number of χ throughout pocket collapse. Decays start immediately, governing the abundance early on in the phase transition. As the radius shrinks, there is less time left in the phase transition to allow for decays to occur, and the abundance due to decays flattens. However, at smaller radii, the density of χ increases enough to enhance the annihilation rate appreciably, allowing for a new depletion process to become relevant.

4.2.1 Boltzmann Equation

We track the abundance of χ throughout the pocket collapse by solving a Boltzmann equation for the number density of χ confined inside the contracting pocket

$$\begin{aligned}\frac{dn_\chi}{dt} + 3\frac{\dot{R}}{R}n_\chi = &- \langle\sigma v\rangle(n_\chi^2 - n_{\rm eq}^2) \\ &- \Gamma_\chi(n_\chi - n_{\rm eq}).\end{aligned} \tag{4.4}$$

We assume that χ have sufficiently strong interactions with the SM plasma that they have their equilibrium abundance at the beginning of the phase transition, and we approximate the pocket to be spherical with a constant wall velocity, v_w. We use a thin-wall approximation since this drastically simplifies the interactions between χ and the bubble wall, while at the cost of a loss on control at the end of the phase transition when the pockets are very small.

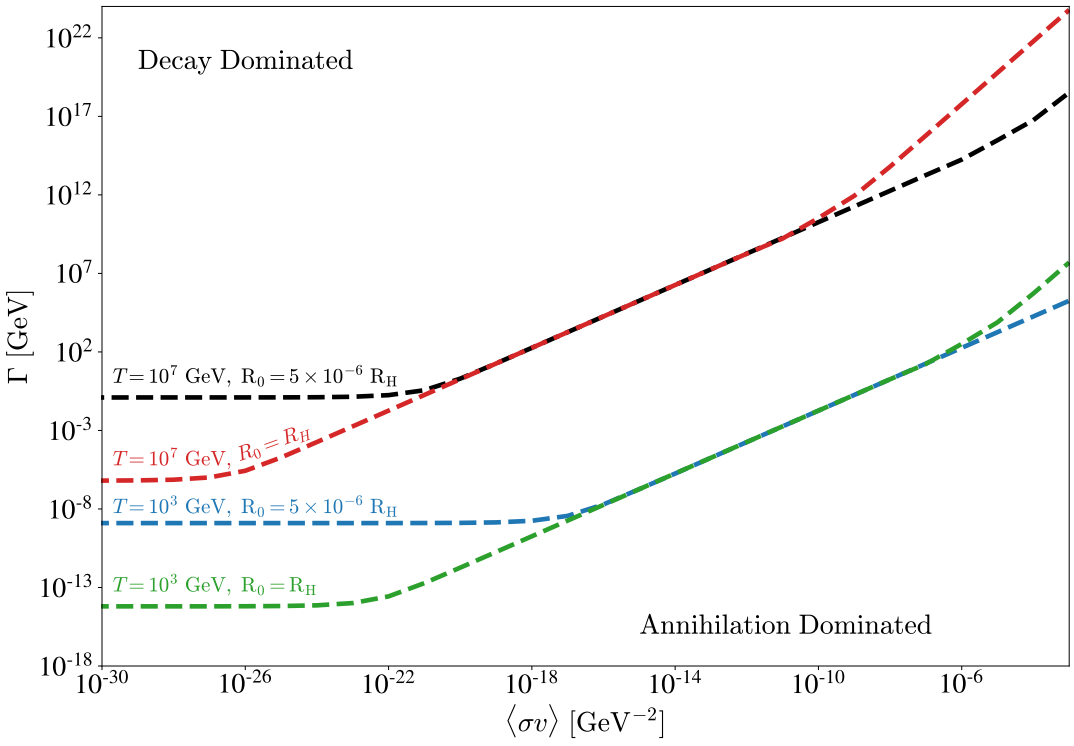

Figure 4.3: Contours in the Γ-$\langle \sigma v \rangle$ plane corresponding to the points where χ is depleted by an equal number of decays and annihilations during the pocket collapse. The four curves correspond to combinations of temperature $T = 10^7$ GeV and initial radius $R_0 = 5 \times 10^{-6} R_H$ (black); $T = 10^7$ GeV and $R_0 = R_H$ (red); $T = 10^3$ GeV and $R_0 = 5 \times 10^{-6} R_H$ (blue); and $T = 10^3$ GeV and $R_0 = R_H$ (green).

However, the dominant processes operate much earlier than when the Boltzmann equation breaks down. The Boltzmann equation can be recast into an equation differential in the radius of the pocket by making use of the relation $\frac{dn_\chi}{dt} = \frac{dn_\chi}{dR}\frac{dR}{dt} = -v_w \frac{dn_\chi}{dR}$,

$$\begin{aligned} -v_w \frac{dn_\chi}{dR} - 3\frac{v_w}{R} n_\chi = &- \langle\sigma v\rangle (n_\chi^2 - n_{\rm eq}^2) \\ &- \Gamma_\chi (n_\chi - n_{\rm eq}). \end{aligned} \tag{4.5}$$

For a generic point in parameter space, both annihilation and decay may be significant.

The total number of χ inside the pocket is $N_\chi = 4\pi R^3 n_\chi/3$, for which:

$$\frac{dN_\chi}{dR} = -\frac{4\pi R^3}{3v_w}\Big(\langle\sigma v\rangle (n_\chi^2 - n_{\rm eq}^2) + \Gamma_\chi (n_\chi - n_{\rm eq})\Big). \tag{4.6}$$

In the Eq. 4.6, we assume that the density is constant throughout the pockets. While there would be some over-densities of χ near the bubble walls, non-relativistic bubble walls would typically expand too slowly to produce a pile-up of relativistic χ. In the case of relativistic bubble walls, where pile-up is more likely to occur, it would in principle enhance the annihilation near the bubble wall, and suppress the annihilation near the centers of the bubbles. The interplay of these two processes could be complicated, and to demonstrate the mechanism, we approximate the density to be uniform throughout the pocket.

To determine the dominant process responsible for depleting the abundance inside the pocket, we compute the fraction of the depletion that was from annihilation, $f_A = \Delta N_{\rm annihilation}/\Delta N_{\rm total}$,

by comparing the integral of the corresponding terms in the Boltzmann equation,

$$f_A = \frac{1}{\Delta N_{\rm total}} \int dN_{\rm annihilation} \tag{4.7}$$
$$= \frac{\displaystyle\int_{R_0}^{1/M} R^3 dR\ \langle\sigma v\rangle (n_\chi^2 - n_{\rm eq}^2)}{\displaystyle\int_{R_0}^{1/M} R^3 dR\ \Big(\langle\sigma v\rangle (n_\chi^2 - n_{\rm eq}^2) + \Gamma_\chi (n_\chi - n_{\rm eq})\Big)}.$$

In Fig. 4.3 we show contours in the plane of Γ-$\langle\sigma v\rangle$ corresponding to equal depletion by decay and annihilation for $v_w = 10^{-3}$, $M_\chi^{\rm in}/T = 10$ and for four different combinations of the initial pocket size R_0 and the temperature T at which the phase transition takes place. Generally as expected, larger widths correspond to decay domination, and larger cross sections to annihilation cross section, with the boundary of $f_A = 1/2$ determined by the temperature, which controls the initial density of χ and thus the rate of annihlation. However, there is a flattening at low $\langle\sigma v\rangle$ which occurs when the decay and annihilation processes are operating during different times. In this case, the decays start immediately and the contour of $f_A = 1/2$ corresponds to the point where half of the initial abundance inside the pocket decays before the time where squeezing becomes sufficient that annihilations turn on and deplete the rest of the abundance.

For a phase transition with different v_w, the dominant difference is through the explicit dependence in equation (4.5), which can be rescaled such that the quantities driving the evolution of n_χ are Γ_χ/v_w and $\langle\sigma v\rangle/v_w$. For larger v_w, in order to keep the χ confined to the pockets, the phase transition must also have a larger value of $M_\chi^{\rm in}/T$ which further implies that the χ reach sufficient Casimir energy to escape the pockets at a smaller pocket radius, and thus there is a slightly longer period for decay and annihilation to operate. For the relativistic wall velocity case we consider with $v_w = 0.9$ and $M_\chi^{\rm in}/T = 10^2$, this second effect is numerically unimportant, and the contours of fixed f_A are very close to those shown in Figure 4.3 with appropriate rescaling by v_w.

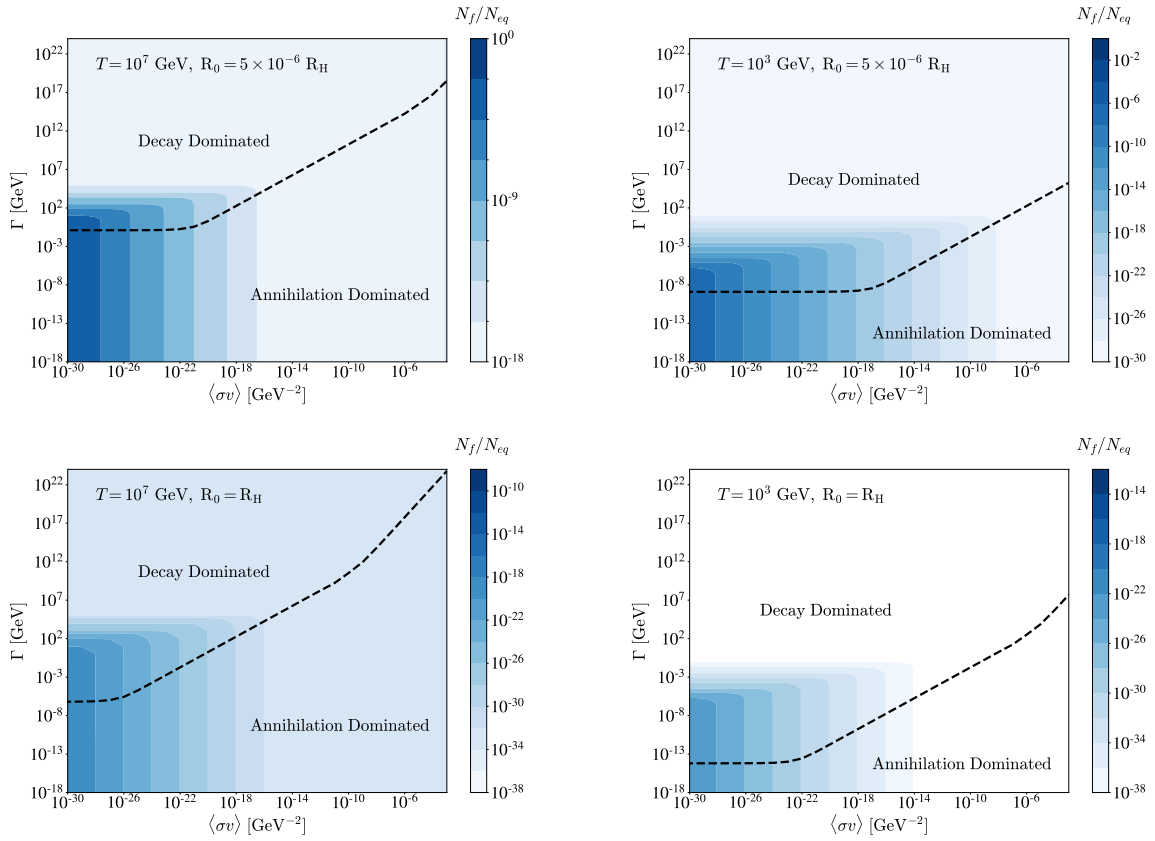

Figure 4.4: Contours in the Γ-$\langle \sigma v \rangle$ plane indicating the fraction of the initial abundance that remains in the unbroken phase when the pocket radius reaches $R = 1/M_\chi^{\rm in}$, for the same four combinations of T and R_0 as in Figure 4.3. The black contours correspond to points shown in Figure 4.3 where $f_A = 1/2$.

Fig. 4.4 displays for each of the parameter sets shown in Fig. 4.3 the total depletion in the plane of Γ-$\langle\sigma v\rangle$. Depletion in very efficient in most of the plane, but in regions with both very small decay widths and annihilation cross sections, there could be a population of χ that survive the pocket collapse.

4.3 Application to Baryogenesis

We consider an application of these results to baryogenesis, continuing to work in a generic framework in which χ particles can both decay and annihilate into SM states, and including the possibility of CP violation (as well as C and baryon-number violation) being present in both processes. As noted above, the specific interactions mediating χ decay or annihilation may be different (and thus have intrinsically different CP violation). Even if the underlying source of CP violation is the same for both processes, they will still generically manifest themselves differently, because of different topologies of loop diagrams that contribute.

We parameterize the asymmetries present in the decay and annihilation processes as ϵ_D and ϵ_A, respectively:

$$\epsilon_D \equiv \frac{\sum_\alpha \left[\Gamma\left(\chi \to \mathrm{SM}\right) - \overline{\Gamma}\left(\chi \to \mathrm{SM}\right)\right]}{\sum_\alpha \left[\Gamma\left(\chi \to \mathrm{SM}\right) + \overline{\Gamma}\left(\chi \to \mathrm{SM}\right)\right]} \tag{4.8}$$

$$\epsilon_A \equiv \frac{\sum_\alpha \left[\sigma\left(\chi\chi \to \mathrm{SM\,SM}\right) - \overline{\sigma}\left(\chi\chi \to \mathrm{SM\,SM}\right)\right]}{\sum_\alpha \left[\sigma\left(\chi\chi \to \mathrm{SM\,SM}\right) + \overline{\sigma}\left(\chi\chi \to \mathrm{SM\,SM}\right)\right]}. \tag{4.9}$$

We assume, as is typically the case, that $\epsilon_D, \epsilon_A \ll 1$.

The asymmetry generated by the combined decay and annihilation processes, $\epsilon_{\mathrm{total}}$, is obtained by integrating the Boltzmann equation, keeping track of the fraction of χ that anni-

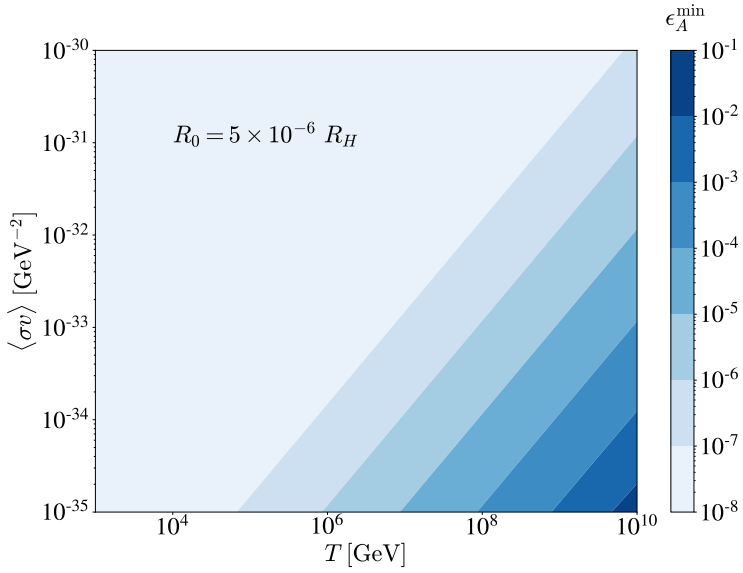

Figure 4.5: The minimum asymmetry needed to be generated by the annihilation processes in the $\langle \sigma v \rangle - T$ plane, in the scenario with $R_0 = 5 \times 10^{-6} R_H$, where annihilation dominates.

hilate versus decay:

$$\begin{aligned} \epsilon_{\text{total}} &= \frac{1}{\Delta N_{\chi,\text{total}}} \int \left(\epsilon_A \frac{dN_{\text{ann}}}{dR} + \epsilon_D \frac{dN_{\text{decay}}}{dR} \right) dR \\ &= \epsilon_A f_A + \epsilon_D (1 - f_A). \end{aligned} \tag{4.10}$$

The resulting baryon asymmetry can be parameterized as:

$$Y_{\Delta B} = \Delta Y_\chi \epsilon_{\text{total}} C = \frac{\Delta n_\chi(T)}{s(T)} \epsilon_{\text{total}} C \tag{4.11}$$

where $Y_i = n_i/s$, Δn_χ is the total change in the number density of χ during the pocket collapse as determined by the Boltzmann equation, Eq. 4.6, $s(T)$ is the entropy density, and C translates from the CP asymmetry present in the χ depletion processes to the final asymmetry in baryons. For example, if χ depletion produces an asymmetry in lepton number that is subsequently converted into a baryon asymmetry via electroweak sphalerons ("leptogenesis"), $C \simeq 12/37$ [55].

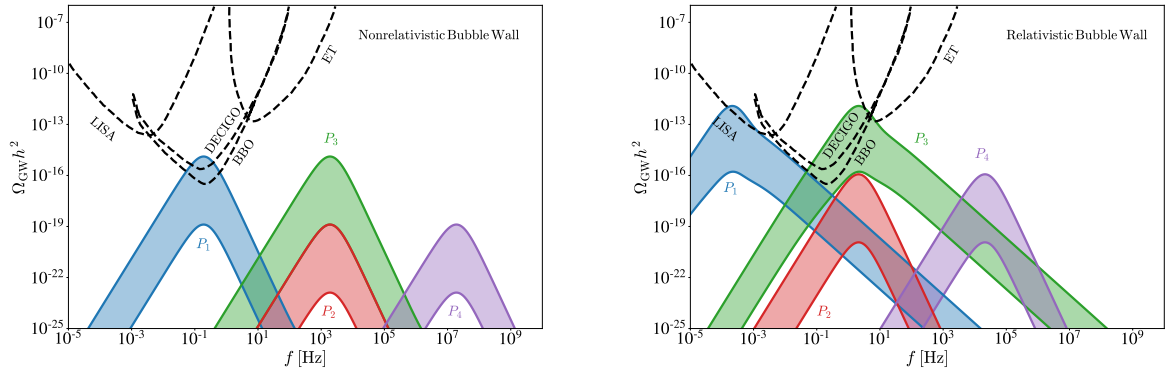

Figure 4.6: Spectrum of stochastic gravitational waves produced by a FOPT. The four bands represent phase transitions with: $(T, \beta_H) = (10^3\,\text{GeV}, 1)$ (P1, blue), $(10^3\,\text{GeV}, 10^4)$ (P2, red), $(10^7\,\text{GeV}, 1)$ (P3, green), and $(10^7\,\text{GeV}, 10^4)$ (P4, purple) with latent heat values $\alpha \geq 0.01$. The black dashed lines show projected experimental reaches from the future experiments LISA, DECIGO, BBO, and ET.

In Fig. 4.5, we display the minimum $\epsilon_A^{\rm min}$ in annihilations that is necessary to produced the observed baryon asymmetry, in the $\langle\sigma v\rangle - T$ plane, for the annihilation-dominated phase transition with $R_0 = 5 \times 10^{-6} R_H$ and $C = 1$. Even for the tiny $\langle\sigma v\rangle$ considered, there is sufficient enhancement provided by the squeezed annihilation rate in much of the parameter space to generate a sufficient baryon asymmetry such that only a rather modest $\epsilon \sim \mathcal{O}(10^{-8})$ is needed.

4.4 Gravitational Waves

A first order phase transition produces a stochastic background of gravitational waves that could be observable. The gravitational wave spectrum is thought to be composed of three primary components,

$$\Omega_{gw}h^2 = \Omega_b h^2 + \Omega_s h^2 + \Omega_t h^2, \tag{4.12}$$

where b, s, and t represent the bubble collision, sound wave, and turbulence contributions to the gravitational wave spectrum, and whose contributions can be estimated in terms of quantities characterizing the properties of the transition itself, α, $\beta_H \equiv \beta/H_*$, T_*, v_w, and κ_i, where:

$$\beta_H = \left(T \frac{\mathrm{d}}{\mathrm{d}T} \left(\frac{S_3(T)}{T} \right) \right) \Bigg|_{T=T_*} . \tag{4.13}$$

These parameters can be estimated based on the properties of the phase transition, and mapped on to the peak amplitudes, frequencies, and spectral shapes of the gravitational wave signal [13], with the spectral shape largely governed by v_w, β_H and T, whereas the amplitude is also sensitive to the latent heat, α and efficiency factors, κ_i. The amplitudes increase for large wall velocities making the relativistic bubble wall case more potentially observable by future experiments.

We sample all values of $\alpha \geq 0.01$ since the amplitudes scale as $(\Omega h^2)^{\mathrm{peak}} \sim (\alpha/(1+\alpha))^n$ with $n > 0$, and the amplitude asymptotically approaches its maximum as $\alpha \gg 1$. We use typical values found in [13] for the efficiencies, $\kappa_b = 10^{-8}$ and $\kappa_v = 10^{-3}$. In Fig. 4.6 , we plot bands that represent the range of sampled α values, and consider four benchmark parameter points for both relativistic and non-relativistic bubble walls with $\beta_H \sim 1$, 10^4, $v_w \sim 0.9$, 10^{-3}, and $T = 10^3$, 10^7 GeV. Also shown are the projected sensitivities of the future GW experiments, LISA [25], DECIGO [83], BBO [51], and ET [70]. Gravitational wave signals generated in this scenario could be discovered for some of the parameter space considered, with phase transitions resulting in relativistic bubble expansion being more easily detectable.

4.5 Conclusions and Outlook

We have explored a novel interplay between decay and annihilation that arises during a first-order phase transition in which the mass of the annihilating/decaying particle receives a large contribution from the phase transition. We find that pocket collapse produces an enhancement of the particle density, and opens up a large range of parameter space where annihilation can be important, which would typically otherwise be dominated by decay. We investigate baryogenesis during this type of scenario, where the decay and annihilation of χ may both separately contribute to generating the observed baryon asymmetry. While this is a novel application, the interplay between annihilation and decay during such a phase transition is interesting in its own right, and may prove useful in other applications as well.

There are many interesting avenues for future exploration. For example, we approximate a constant temperature of the thermal bath throughout the phase transition, but this need not be the case. Indeed, the duration of the phase transition is longer than the Hubble scale for pockets whose sizes are initially $\sim R_H$, such that the temperature of the universe may cool appreciably. Other types of phase transition may themselves generate significant amounts of heating. We further assumed a constant bubble wall velocity, but depending on the heating during the phase transition, and the pressure exerted on the bubble wall by χ could lead to a non-trivial wall velocity profile. Studying this more complicated evolution is left for future work.

It would also be interesting to move beyond generic characterizations and see how these results could be applied to specific models of baryogenesis. For example, χ could be a right handed neutrino in a seesaw model of neutrino masses, whose large mass could be the result of the vacuum expectation value of a field spontaneously breaking lepton number. Typically in leptogenesis models, decays dominate and annihilation is negligible; but for the an appropriate type of phase transition this expectation could be upset, leading to a different

mapping between the phases of the neutrino masses and Yukawa couplings and the resulting baryon asymmetry (from annihilating sterile neutrinos), and violating the Davidson-Ibarra bound [54], or the need for tiny mass differences required by resonant leptogenesis [108].

If the χ is stable, it could play the role of dark matter, and it might be possible to generate the observed dark matter relic abundance and baryon asymmetry at the same time [52, 53]. Even without addressing baryogenesis, the enhancement of the annihilation could relax the relationship between the annihilation cross section and the mass implied by freeze-out production of the dark matter, allowing small values of the cross section to generate the correct amount of dark matter. We leave the investigation of these ideas for future work.

Chapter 5

Conclusions

In this work, we have explored non-standard mechanisms and assumptions that lead to differing stories in dark matter and baryogenesis. This took the form of developing novel mechanisms, as well as revisiting assumptions and reevaluating which regions of parameter space are interesting for well-studied models.

In chapter 2, we outline a solution to the strong CP problem which depends on the environment of dark matter. The coherent alignment of spins in a direction specified by the QCD potential dynamically cancels the QCD $\overline{\theta}$ parameter in regions rich with dark matter. This leads to interesting phenomenology, e.g. the spatially varying neutron EDM due to distant CP violation.

In chapter 3, we broaden the typical WIMP parameter space by abandoning the standard WIMP miracle, remaining agnostic to the possibility of different production mechanisms in non-standard cosmologies. With this in mind, we determine the current day constraints from direct detection, indirect detection, and production at colliders. The results we derive must therefore be constraints that any real $SU(2)_{\rm EW}$ triplet scalar WIMP must satisfy, independent of the physics in the early universe.

In chapter 4, we present a new route to baryogenesis, which relies on a strongly first order phase transition. We introduce a new fermion χ, whose decays and annihilations may generally violate CP, and therefore can lead to a baryon asymmetry. The bubbles which nucleate during the phase transition trap the χ in the false vacuum, leading annihilation to be enhanced as they bubbles expand and squeeze the χ together. In general, the topologies of the decay and annihilation diagrams are different, and the CP violation are not constrained to be the same. The interplay between these two processes opens up new regions in the parameter space.

It will be important in the future to continue to relax assumptions and explore non-standard mechanisms to fully explore the space of ideas in BSM physics.

Bibliography

[1] G. Aad et al. Search for dark matter candidates and large extra dimensions in events with a jet and missing transverse momentum with the ATLAS detector. *JHEP*, 04:075, 2013.

[2] G. Aad et al. Search for direct production of charginos, neutralinos and sleptons in final states with two leptons and missing transverse momentum in pp collisions at $\sqrt{s} =$ 8 TeV with the ATLAS detector. *JHEP*, 05:071, 2014.

[3] G. Aad et al. Search for electroweak production of charginos and sleptons decaying into final states with two leptons and missing transverse momentum in $\sqrt{s} = 13$ TeV pp collisions using the ATLAS detector. *Eur. Phys. J. C*, 80(2):123, 2020.

[4] K. N. Abazajian and J. Harding. Constraints on WIMP and Sommerfeld-Enhanced Dark Matter Annihilation from HESS Observations of the Galactic Center. *JCAP*, 01:041, 2012.

[5] H. Abdalla et al. Searches for gamma-ray lines and 'pure WIMP' spectra from Dark Matter annihilations in dwarf galaxies with H.E.S.S. *JCAP*, 11:037, 2018.

[6] H. Abdallah et al. Search for dark matter annihilations towards the inner Galactic halo from 10 years of observations with H.E.S.S. *Phys. Rev. Lett.*, 117(11):111301, 2016.

[7] H. Abdallah et al. Search for γ-Ray Line Signals from Dark Matter Annihilations in the Inner Galactic Halo from 10 Years of Observations with H.E.S.S. *Phys. Rev. Lett.*, 120(20):201101, 2018.

[8] M. Ackermann et al. Searching for Dark Matter Annihilation from Milky Way Dwarf Spheroidal Galaxies with Six Years of Fermi Large Area Telescope Data. *Phys. Rev. Lett.*, 115(23):231301, 2015.

[9] F. C. Adams. General solutions for tunneling of scalar fields with quartic potentials. *Phys. Rev. D*, 48:2800–2805, 1993.

[10] N. Aghanim et al. Planck 2018 results. VI. Cosmological parameters. *Astron. Astrophys.*, 641:A6, 2020.

[11] P. Agrawal, N. Kitajima, M. Reece, T. Sekiguchi, and F. Takahashi. Relic Abundance of Dark Photon Dark Matter. 2018.

[12] D. Akerib et al. Projected WIMP sensitivity of the LUX-ZEPLIN dark matter experiment. *Phys. Rev. D*, 101(5):052002, 2020.

[13] T. Alanne, T. Hugle, M. Platscher, and K. Schmitz. A fresh look at the gravitational-wave signal from cosmological phase transitions. *JHEP*, 03:004, 2020.

[14] J. M. Alarcon, L. S. Geng, J. Martin Camalich, and J. A. Oller. The strangeness content of the nucleon from effective field theory and phenomenology. *Phys. Lett. B*, 730:342–346, 2014.

[15] J. M. Alarcon, J. Martin Camalich, and J. A. Oller. The chiral representation of the πN scattering amplitude and the pion-nucleon sigma term. *Phys. Rev. D*, 85:051503, 2012.

[16] F. Ambrogi, C. Arina, M. Backovic, J. Heisig, F. Maltoni, L. Mantani, O. Mattelaer, and G. Mohlabeng. MadDM v.3.0: a Comprehensive Tool for Dark Matter Studies. *Phys. Dark Univ.*, 24:100249, 2019.

[17] S. Ando, A. Geringer-Sameth, N. Hiroshima, S. Hoof, R. Trotta, and M. G. Walker. Structure formation models weaken limits on WIMP dark matter from dwarf spheroidal galaxies. *Phys. Rev. D*, 102(6):061302, 2020.

[18] E. Aprile et al. Dark Matter Search Results from a One Ton-Year Exposure of XENON1T. *Phys. Rev. Lett.*, 121(11):111302, 2018.

[19] J. Arakawa, A. Rajaraman, and T. M. P. Tait. Emergent Solution to the Strong CP Problem. *Phys. Rev. Lett.*, 123(16):161602, 2019.

[20] J. Arakawa, A. Rajaraman, and T. M. P. Tait. Annihilogenesis. 9 2021.

[21] J. Arakawa and T. M. P. Tait. Is a Miracle-less WIMP Ruled out? *SciPost Phys.*, 11(2):019, 2021.

[22] P. Arias, D. Cadamuro, M. Goodsell, J. Jaeckel, J. Redondo, and A. Ringwald. WISPy Cold Dark Matter. *JCAP*, 1206:013, 2012.

[23] N. Arkani-Hamed, D. P. Finkbeiner, T. R. Slatyer, and N. Weiner. A Theory of Dark Matter. *Phys. Rev. D*, 79:015014, 2009.

[24] P. Asadi, E. D. Kramer, E. Kuflik, G. W. Ridgway, T. R. Slatyer, and J. Smirnov. Thermal Squeezeout of Dark Matter. 3 2021.

[25] P. Auclair et al. Probing the gravitational wave background from cosmic strings with LISA. *JCAP*, 04:034, 2020.

[26] A. Azatov, M. Vanvlasselaer, and W. Yin. Baryogenesis via relativistic bubble walls. 6 2021.

[27] A. Azatov, M. Vanvlasselaer, and W. Yin. Dark Matter production from relativistic bubble walls. *JHEP*, 03:288, 2021.

[28] Y. Bai, P. J. Fox, and R. Harnik. The Tevatron at the Frontier of Dark Matter Direct Detection. *JHEP*, 12:048, 2010.

[29] M. J. Baker, M. Breitbach, J. Kopp, and L. Mittnacht. Primordial Black Holes from First-Order Cosmological Phase Transitions. 5 2021.

[30] M. J. Baker, J. Kopp, and A. J. Long. Filtered Dark Matter at a First Order Phase Transition. *Phys. Rev. Lett.*, 125(15):151102, 2020.

[31] I. Baldes, S. Blasi, A. Mariotti, A. Sevrin, and K. Turbang. Baryogenesis via relativistic bubble expansion. 6 2021.

[32] P. Bandyopadhyay and A. Costantini. The Obscurum Higgs at Colliders. 10 2020.

[33] B. Bar-Or, J.-B. Fouvry, and S. Tremaine. Relaxation in a Fuzzy Dark Matter Halo. *Astrophys. J.*, 871:28, 2019.

[34] B. Barman, P. Ghosh, F. S. Queiroz, and A. K. Saha. Scalar Multiplet Dark Matter in a Fast Expanding Universe: resurrection of the {\it desert} region. 1 2021.

[35] M. Bastero-Gil, J. Santiago, L. Ubaldi, and R. Vega-Morales. Vector dark matter production at the end of inflation. *JCAP*, 1904(04):015, 2019.

[36] M. Battaglieri et al. US Cosmic Visions: New Ideas in Dark Matter 2017: Community Report. In *U.S. Cosmic Visions: New Ideas in Dark Matter College Park, MD, USA, March 23-25, 2017*, 2017.

[37] D. Bauer et al. Dark Matter in the Coming Decade: Complementary Paths to Discovery and Beyond. *Phys. Dark Univ.*, 7-8:16–23, 2015.

[38] D. Berger, S. Ipek, T. M. Tait, and M. Waterbury. Dark Matter Freeze Out during an Early Cosmological Period of QCD Confinement. 4 2020.

[39] G. Bertone and M. Tait, Tim. A new era in the search for dark matter. *Nature*, 562(7725):51–56, 2018.

[40] C. Blanco, M. Escudero, D. Hooper, and S. J. Witte. Z' mediated WIMPs: dead, dying, or soon to be detected? *JCAP*, 11:024, 2019.

[41] C. Burgess, M. Pospelov, and T. ter Veldhuis. The Minimal model of nonbaryonic dark matter: A Singlet scalar. *Nucl. Phys. B*, 619:709–728, 2001.

[42] A. Burkert. The Structure of dark matter halos in dwarf galaxies. *IAU Symp.*, 171:175, 1996.

[43] M. Carena, M. Quiros, and C. E. M. Wagner. Opening the window for electroweak baryogenesis. *Phys. Lett. B*, 380:81–91, 1996.

[44] T. Chan, D. Kereˇ s, J. Oñorbe, P. Hopkins, A. Muratov, C. A. Faucher-Giguère, and E. Quataert. The impact of baryonic physics on the structure of dark matter haloes: the view from the FIRE cosmological simulations. *Mon. Not. Roy. Astron. Soc.*, 454(3):2981–3001, 2015.

[45] C.-W. Chiang, G. Cottin, Y. Du, K. Fuyuto, and M. J. Ramsey-Musolf. Collider Probes of Real Triplet Scalar Dark Matter. 3 2020.

[46] D. Chway, T. H. Jung, and C. S. Shin. Dark matter filtering-out effect during a first-order phase transition. *Phys. Rev. D*, 101(9):095019, 2020.

[47] M. Cirelli, N. Fornengo, and A. Strumia. Minimal dark matter. *Nucl. Phys. B*, 753:178–194, 2006.

[48] R. T. Co, A. Pierce, Z. Zhang, and Y. Zhao. Dark Photon Dark Matter Produced by Axion Oscillations. *Phys. Rev.*, D99(7):075002, 2019.

[49] A. G. Cohen, D. B. Kaplan, and A. E. Nelson. Progress in electroweak baryogenesis. *Ann. Rev. Nucl. Part. Sci.*, 43:27–70, 1993.

[50] T. Cohen, M. Lisanti, A. Pierce, and T. R. Slatyer. Wino Dark Matter Under Siege. *JCAP*, 10:061, 2013.

[51] V. Corbin and N. J. Cornish. Detecting the cosmic gravitational wave background with the big bang observer. *Class. Quant. Grav.*, 23:2435–2446, 2006.

[52] Y. Cui, L. Randall, and B. Shuve. Emergent Dark Matter, Baryon, and Lepton Numbers. *JHEP*, 08:073, 2011.

[53] Y. Cui, L. Randall, and B. Shuve. A WIMPy Baryogenesis Miracle. *JHEP*, 04:075, 2012.

[54] S. Davidson and A. Ibarra. A Lower bound on the right-handed neutrino mass from leptogenesis. *Phys. Lett. B*, 535:25–32, 2002.

[55] S. Davidson, E. Nardi, and Y. Nir. Leptogenesis. *Phys. Rept.*, 466:105–177, 2008.

[56] M. Dine, W. Fischler, and M. Srednicki. A Simple Solution to the Strong CP Problem with a Harmless Axion. *Phys. Lett.*, 104B:199–202, 1981.

[57] J. A. Dror, K. Harigaya, and V. Narayan. Parametric Resonance Production of Ultralight Vector Dark Matter. *Phys. Rev.*, D99(3):035036, 2019.

[58] D. Egana-Ugrinovic, M. Low, and J. T. Ruderman. Charged Fermions Below 100 GeV. *JHEP*, 05:012, 2018.

[59] J. Ellis, N. Nagata, and K. A. Olive. Uncertainties in WIMP Dark Matter Scattering Revisited. *Eur. Phys. J. C*, 78(7):569, 2018.

[60] J. Fan and M. Reece. In Wino Veritas? Indirect Searches Shed Light on Neutralino Dark Matter. *JHEP*, 10:124, 2013.

[61] J. L. Feng and J. Kumar. The WIMPless Miracle: Dark-Matter Particles without Weak-Scale Masses or Weak Interactions. *Phys. Rev. Lett.*, 101:231301, 2008.

[62] G. B. Gelmini and P. Gondolo. Neutralino with the right cold dark matter abundance in (almost) any supersymmetric model. *Phys. Rev. D*, 74:023510, 2006.

[63] J. Goodman, M. Ibe, A. Rajaraman, W. Shepherd, T. M. P. Tait, and H.-B. Yu. Constraints on Dark Matter from Colliders. *Phys. Rev.*, D82:116010, 2010.

[64] A. W. Graham, D. Merritt, B. Moore, J. Diemand, and B. Terzic. Empirical models for Dark Matter Halos. I. Nonparametric Construction of Density Profiles and Comparison with Parametric Models. *Astron. J.*, 132:2685–2700, 2006.

[65] P. W. Graham, J. Mardon, and S. Rajendran. Vector Dark Matter from Inflationary Fluctuations. *Phys. Rev.*, D93(10):103520, 2016.

[66] C. Gross, G. Landini, A. Strumia, and D. Teresi. Dark Matter as dark dwarfs and other macroscopic objects: multiverse relics? *JHEP*, 09:033, 2021.

[67] M. Grossi and V. Springel. The impact of Early Dark Energy on non-linear structure formation. *Mon. Not. Roy. Astron. Soc.*, 394:1559–1574, 2009.

[68] T. Hambye, A. Strumia, and D. Teresi. Super-cool Dark Matter. *JHEP*, 08:188, 2018.

[69] S. Hamdan and J. Unwin. Dark Matter Freeze-out During Matter Domination. *Mod. Phys. Lett. A*, 33(29):1850181, 2018.

[70] S. Hild et al. Sensitivity Studies for Third-Generation Gravitational Wave Observatories. *Class. Quant. Grav.*, 28:094013, 2011.

[71] R. J. Hill and M. P. Solon. Universal behavior in the scattering of heavy, weakly interacting dark matter on nuclear targets. *Phys. Lett. B*, 707:539–545, 2012.

[72] J. Hisano, K. Ishiwata, and N. Nagata. A complete calculation for direct detection of Wino dark matter. *Phys. Lett. B*, 690:311–315, 2010.

[73] J. Hisano, S. Matsumoto, M. M. Nojiri, and O. Saito. Non-perturbative effect on dark matter annihilation and gamma ray signature from galactic center. *Phys. Rev. D*, 71:063528, 2005.

[74] J.-P. Hong, S. Jung, and K.-P. Xie. Fermi-ball dark matter from a first-order phase transition. *Phys. Rev. D*, 102(7):075028, 2020.

[75] W. Hu, R. Barkana, and A. Gruzinov. Cold and fuzzy dark matter. *Phys. Rev. Lett.*, 85:1158–1161, 2000.

[76] F. P. Huang and C. S. Li. Probing the baryogenesis and dark matter relaxed in phase transition by gravitational waves and colliders. *Phys. Rev. D*, 96(9):095028, 2017.

[77] L. Hui, J. P. Ostriker, S. Tremaine, and E. Witten. Ultralight scalars as cosmological dark matter. *Phys. Rev.*, D95(4):043541, 2017.

[78] C. Jackson, G. Servant, G. Shaughnessy, T. M. Tait, and M. Taoso. Gamma-ray lines and One-Loop Continuum from s-channel Dark Matter Annihilations. *JCAP*, 07:021, 2013.

[79] E. Karukes, M. Benito, F. Iocco, R. Trotta, and A. Geringer-Sameth. Bayesian reconstruction of the milky way dark matter distribution. *Journal of Cosmology and Astroparticle Physics*, 2019(09):046–046, Sep 2019.

[80] K. Kawana and K.-P. Xie. Primordial black holes from a cosmic phase transition: The collapse of Fermi-balls. 5 2021.

[81] J. Kehayias and S. Profumo. Semi-Analytic Calculation of the Gravitational Wave Signal From the Electroweak Phase Transition for General Quartic Scalar Effective Potentials. *JCAP*, 03:003, 2010.

[82] J. E. Kim. Weak Interaction Singlet and Strong CP Invariance. *Phys. Rev. Lett.*, 43:103, 1979.

[83] H. Kudoh, A. Taruya, T. Hiramatsu, and Y. Himemoto. Detecting a gravitational-wave background with next-generation space interferometers. *Phys. Rev. D*, 73:064006, 2006.

[84] V. A. Kuzmin, V. A. Rubakov, and M. E. Shaposhnikov. On the Anomalous Electroweak Baryon Number Nonconservation in the Early Universe. *Phys. Lett. B*, 155:36, 1985.

[85] R. K. Leane, T. R. Slatyer, J. F. Beacom, and K. C. Ng. GeV-scale thermal WIMPs: Not even slightly ruled out. *Phys. Rev. D*, 98(2):023016, 2018.

[86] B. W. Lee and S. Weinberg. Cosmological Lower Bound on Heavy Neutrino Masses. *Phys. Rev. Lett.*, 39:165–168, 1977.

[87] T. Lin. Dark matter models and direct detection. *PoS*, 333:009, 2019.

[88] H. Liu, G. W. Ridgway, and T. R. Slatyer. Code package for calculating modified cosmic ionization and thermal histories with dark matter and other exotic energy injections. *Phys. Rev. D*, 101(2):023530, 2020.

[89] H. Liu and T. R. Slatyer. Implications of a 21-cm signal for dark matter annihilation and decay. *Phys. Rev. D*, 98(2):023501, 2018.

[90] D. Marfatia and P.-Y. Tseng. Correlated gravitational wave and microlensing signals of macroscopic dark matter. 7 2021.

[91] D. Marfatia and P.-Y. Tseng. Gravitational wave signals of dark matter freeze-out. *JHEP*, 02:022, 2021.

[92] D. J. E. Marsh and J. C. Niemeyer. Strong Constraints on Fuzzy Dark Matter from Ultrafaint Dwarf Galaxy Eridanus II. 2018.

[93] A. Mégevand and S. Ramírez. Bubble nucleation and growth in slow cosmological phase transitions. *Nucl. Phys. B*, 928:38–71, 2018.

[94] E. Mereghetti, J. de Vries, W. H. Hockings, C. M. Maekawa, and U. van Kolck. The Electric Dipole Form Factor of the Nucleon in Chiral Perturbation Theory to Subleading Order. *Phys. Lett.*, B696:97–102, 2011.

[95] P. Mollitor, E. Nezri, and R. Teyssier. Baryonic and dark matter distribution in cosmological simulations of spiral galaxies. *Mon. Not. Roy. Astron. Soc.*, 447(2):1353–1369, 2015.

[96] H. Murayama. `http://hitoshi.berkeley.edu/221B-S01/finalsol.pdf`. (2001).

[97] E. O. Nadler, V. Gluscevic, K. K. Boddy, and R. H. Wechsler. Constraints on Dark Matter Microphysics from the Milky Way Satellite Population. 2019.

[98] O. Nebrin, R. Ghara, and G. Mellema. Fuzzy Dark Matter at Cosmic Dawn: New 21-cm Constraints. 2018.

[99] A. E. Nelson and J. Scholtz. Dark Light, Dark Matter and the Misalignment Mechanism. *Phys. Rev.*, D84:103501, 2011.

[100] F. Nesti and P. Salucci. The Dark Matter halo of the Milky Way, AD 2013. *JCAP*, 07:016, 2013.

[101] K. A. Olive. The thermodynamics of the quark-hadron phase transition in the early universe. *Nuclear Physics B*, 190(3):483–503, 1981.

[102] R. D. Peccei and H. R. Quinn. Constraints Imposed by CP Conservation in the Presence of Instantons. *Phys. Rev.*, D16:1791–1797, 1977.

[103] R. D. Peccei and H. R. Quinn. CP Conservation in the Presence of Instantons. *Phys. Rev. Lett.*, 38:1440–1443, 1977. [,328(1977)].

[104] J. M. Pendlebury et al. Revised experimental upper limit on the electric dipole moment of the neutron. *Phys. Rev.*, D92(9):092003, 2015.

[105] M. Petač, P. Ullio, and M. Valli. On velocity-dependent dark matter annihilations in dwarf satellites. *Journal of Cosmology and Astroparticle Physics*, 2018(12):039–039, Dec 2018.

[106] A. Pierce, K. Riles, and Y. Zhao. Searching for Dark Photon Dark Matter with Gravitational Wave Detectors. *Phys. Rev. Lett.*, 121(6):061102, 2018.

[107] L. Pieri, J. Lavalle, G. Bertone, and E. Branchini. Implications of high-resolution simulations on indirect dark matter searches. *Phys. Rev. D*, 83:023518, Jan 2011.

[108] A. Pilaftsis. CP violation and baryogenesis due to heavy Majorana neutrinos. *Phys. Rev. D*, 56:5431–5451, 1997.

[109] A. Rajaraman, T. M. Tait, and A. M. Wijangco. Effective Theories of Gamma-ray Lines from Dark Matter Annihilation. *Phys. Dark Univ.*, 2:17–21, 2013.

[110] L. Rinchiuso, N. L. Rodd, I. Moult, E. Moulin, M. Baumgart, T. Cohen, T. R. Slatyer, I. W. Stewart, and V. Vaidya. Hunting for Heavy Winos in the Galactic Center. *Phys. Rev. D*, 98(12):123014, 2018.

[111] A. D. Sakharov. Violation of CP Invariance, C asymmetry, and baryon asymmetry of the universe. *Pisma Zh. Eksp. Teor. Fiz.*, 5:32–35, 1967.

[112] J. J. Sakurai. *Advanced quantum mechanics*. Addison-Wesley Publishing Company, Chicago, 1967.

[113] S. Schlamminger, K. Y. Choi, T. A. Wagner, J. H. Gundlach, and E. G. Adelberger. Test of the equivalence principle using a rotating torsion balance. *Phys. Rev. Lett.*, 100:041101, 2008.

[114] M. Sher. Electroweak Higgs Potentials and Vacuum Stability. *Phys. Rept.*, 179:273–418, 1989.

[115] M. A. Shifman, A. I. Vainshtein, and V. I. Zakharov. Can Confinement Ensure Natural CP Invariance of Strong Interactions? *Nucl. Phys.*, B166:493–506, 1980.

[116] A. M. Sirunyan et al. Searches for pair production of charginos and top squarks in final states with two oppositely charged leptons in proton-proton collisions at $\sqrt{s} = 13$ TeV. *JHEP*, 11:079, 2018.

[117] A. M. Sirunyan et al. Measurements of the Higgs boson width and anomalous HVV couplings from on-shell and off-shell production in the four-lepton final state. *Phys. Rev. D*, 99(11):112003, 2019.

[118] A. M. Sirunyan et al. Search for invisible decays of a Higgs boson produced through vector boson fusion in proton-proton collisions at $\sqrt{s} = 13$ TeV. *Phys. Lett. B*, 793:520–551, 2019.

[119] T. R. Slatyer. Indirect dark matter signatures in the cosmic dark ages. I. Generalizing the bound on s-wave dark matter annihilation from Planck results. *Phys. Rev. D*, 93(2):023527, 2016.

[120] T. R. Slatyer and C.-L. Wu. General Constraints on Dark Matter Decay from the Cosmic Microwave Background. *Phys. Rev. D*, 95(2):023010, 2017.

[121] M. Srednicki. *Quantum field theory*. Cambridge University Press, 2007.

[122] Y. Su, B. R. Heckel, E. G. Adelberger, J. H. Gundlach, M. Harris, G. L. Smith, and H. E. Swanson. New tests of the universality of free fall. *Phys. Rev.*, D50:3614–3636, 1994.

[123] S. Tremaine and J. E. Gunn. Dynamical role of light neutral leptons in cosmology. *Phys. Rev. Lett.*, 42:407–410, Feb 1979.

[124] L. Ubaldi. Effects of theta on the deuteron binding energy and the triple-alpha process. *Phys. Rev.*, D81:025011, 2010.

[125] S. S. Vogt et al. HIRES: the high-resolution echelle spectrometer on the Keck 10-m Telescope. *Proc. SPIE Int. Soc. Opt. Eng.*, 2198:362, 1994.

[126] S. Weinberg. A New Light Boson? *Phys. Rev. Lett.*, 40:223–226, 1978.

[127] F. Wilczek. Problem of Strong P and T Invariance in the Presence of Instantons. *Phys. Rev. Lett.*, 40:279–282, 1978.

[128] E. Witten. Cosmological Consequences of a Light Higgs Boson. *Nucl. Phys. B*, 177:477–488, 1981.

[129] E. Witten. Cosmic separation of phases. *Phys. Rev. D*, 30:272–285, Jul 1984.

[130] A. R. Zhitnitsky. On Possible Suppression of the Axion Hadron Interactions. (In Russian). *Sov. J. Nucl. Phys.*, 31:260, 1980. [Yad. Fiz.31,497(1980)].